JGR Solid Earth

Key Points:

- Seventeen percent of calculated full moment tensors in southern Kansas contain significant volumetric components
- Areas containing significant volumetric components are localized around the epicentral location of the largest earthquakes
- Around the 2014 M_W 4.9 Milan earthquake, σ_{Hmax} is rotated 25° clockwise with respect to the average orientation in the study area

Supporting Information:

Supporting Information may be found in the online version of this article.

Correspondence to:

A. Amemoutou,
amandine@gfz-potsdam.de

Earthquake Source Mechanisms and Stress Field Variations Associated With Wastewater-Induced Seismicity in Southern Kansas, USA

Amandine Amemoutou[1] , **Patricia Martínez-Garzón[1]** , **Grzegorz Kwiatek[1]** , **Justin L. Rubinstein[2]** , and **Marco Bohnhoff[1,3]**

[1]Geomechanics and Scientific Drilling, Helmholtz Centre Potsdam, GFZ German Research Centre for Geosciences, Potsdam, Germany, [2]U.S. Geological Survey, Menlo Park, CA, USA, [3]Institute of Geological Sciences, Free University of Berlin, Berlin, Germany

Abstract The strong increase of seismicity rates in the contiguous USA over the last 10 years is linked to the injection of huge amounts of wastewater from oil and gas production in unconventional hydrocarbon reservoirs. We calculated 549 moment tensors of induced earthquakes ($M_W \leq 4.9$) in southern Kansas to study their source mechanisms and their relation to injection activity. Seventeen percent of the events analyzed contained significant volumetric (ISO%) components, and these events mostly occurred near the two largest local earthquakes during the 4 months of largest active wastewater disposal. Mapping the local stress field, we determined that most of the region lies within a transtensional stress regime, with a maximum horizontal stress σ_{Hmax} trending N75°E. In the epicentral area of the M_W 4.9 Milan earthquake, the σ_{Hmax} trend is rotated to about S80°E. Locally, two areas display a change in the stress field orientation with depth, from transtensional above 5.5 km depth to strike slip deeper in the basement. Relating the resolved fault geometries to the obtained local stress field orientation, we find that most of the activated fault planes were optimally oriented to the current stress field and thus small stress perturbations caused by the water injection could lead to failure.

Plain Language Summary The extraction of oil and gas from unconventional hydrocarbon reservoirs creates a huge amount of waste salt water commonly reinjected in the crust. The strong increase in the seismicity rates of the contiguous USA over the last 10 years is linked to these enormous quantities of injected fluids. To understand the processes linked to this induced seismicity, we studied the source processes of 549 earthquakes with small to moderate magnitudes M_L [1.9, 4.9] in southern Kansas and their link to the injection activity. We find that 17% of the earthquakes contain larger proportion of opening and closing processes than typical crustal tectonic earthquakes. Mapping the local stress field provides information on the orientation and regime of the forces exerted in the crust. The direction (strike) in which the forces are larger is NNE-SSW. In the area where the largest local earthquake occurred, the 2014 M_L 4.9 Milan earthquake, the stress field rotated clockwise of about 25°. Locally, two areas display a change in the stress field orientation around 5.5 km depth in the basement. Finally, we find that small stress perturbations caused by the water injection could be sufficient to reactivate most of the faults in the study area.

1. Introduction

During the last decade, seismicity in the central USA, and particularly in Oklahoma and Kansas, drastically increased due to the rapid development of unconventional oil and gas fields (Ellsworth, 2013; Ellsworth et al., 2015; Rubinstein et al., 2018). The primary cause of the elevated seismicity rates is the underground injection of large volumes of wastewater that are a byproduct of the oil and gas production (Ellsworth et al., 2015; Walsh & Zoback, 2015; Weingarten et al., 2015). The injection of large volumes of wastewater results in perturbations of the pore fluid pressure and changes in local stress conditions in the vicinity of the wells and beyond. Over time and due to extremely large volumes injected, this led to downward migration of fluids, partly along preexisting fractures, and ultimately to the reactivation of critically stressed faults deeper in the crystalline basement (e.g., McNamara et al., 2015; Rubinstein & Mahani, 2015). As seismicity occurred at larger (>10 km) distances from the main wastewater disposal area, stress transfer

from earthquake interaction has been suggested to play a role in triggering additional seismicity in the area (Cochran et al., 2018). Poroelastic effects are also believed to induce seismicity (Barbour et al., 2017; Goebel et al., 2017). Because the stress changes from all of the aforementioned effects are rather small, critically stressed faults optimally oriented with respect to the local stress field conditions have a higher probability of failure (e.g., Walsh & Zoback, 2015).

Even within a homogeneous stress field, preexisting faults with different geometries can be reactivated (McKenzie, 1969). If present, optimally oriented faults with respect to the local stress fields are the first to fail in response to a pore pressure increase from fluid injection, as they require a smaller stress change to be reactivated than faults with less favorable geometries and larger pore pressures are necessary to induce earthquakes on nonoptimally oriented faults (e.g., Joubert et al., 2020; Martínez-Garzón et al., 2016).

In the central USA, the largest seismicity rates have been registered in Oklahoma. Most of the seismicity is located in the upper part of the crystalline basement (<6 km depth), activating subvertical strike-slip faults (McNamara et al., 2015). Generally, these faults were found to be favorably oriented (NE-SW and NW-SE) for failure within the regional stress field. Techniques such as slip tendency analyses are able to identify those faults with larger potential for activation (e.g., Moeck et al., 2009; Morris et al., 1996; Schwab et al., 2017). Walsh and Zoback (2016) defined a probabilistic method to assess the probability of fault reactivation, based on known fault orientation and assumptions of the geomechanical conditions, and they determined two main trends of active faults. Both techniques require a priori information on the complete state of stress (orientation and magnitudes of principal stress axes), which is often unknown. In the case of slip tendency, Atkinson et al. (2020) discussed the limitation of this approach, which assumes existing mapped faults and known locations and geometries whereas it is common for induced earthquakes to occur on previously unmapped faults (Schultz et al., 2020), which is the case here. An alternative approach is to determine how well oriented (or how "unstable") a fault is with respect to the stress field orientation, which has the advantage that only information on the stress field orientation and the friction coefficient is needed (e.g., Vavryčuk, 2011, 2014).

The majority of tectonic earthquakes are well characterized with a pure shear double-couple (DC) source. However, non-DC components representing crack opening or closing (isotropic [ISO]), or complex nonlinear rupture surfaces (compensated linear vector dipole [CLVD]) have been observed in areas of fluid injection and extraction due to the pore pressure changes caused by these processes (Jost & Herrmann, 1989). Examples of induced seismicity with significant non-DC components have been reported during hydraulic fracturing operations in Canada (Wang et al., 2018; Zhang et al., 2019), geothermal energy production at The Geysers and Salton Sea geothermal fields in California (Bentz et al., 2018; Martínez-Garzón et al., 2017), and in scientific injection experiments at the Äspö underground research laboratory in Sweden (Kwiatek et al., 2018).

While well characterized moment tensors (MTs) are available for many areas with high rates of induced seismicity, there are only few observations in Oklahoma and even less in southern Kansas, the areas with the most intense-induced seismicity during the last few years, thus limiting the ability to understand the local stress field variability. To this end, we here present the first high-quality catalog of MTs for wastewater disposal-induced seismicity in southern Kansas. We calculated and analyzed MTs for 549 induced earthquakes in this region. Subsequently, we inverted the obtained focal mechanisms (DC part of the MTs) to determine the stress field orientation within the region and any spatial variability. Finally, we then assessed how well oriented the activated faults are in the obtained local stress field.

2. Study Area, Earthquake Catalog, and Waveform Data Processing

The area comprising the border between southern Kansas and Oklahoma is situated within the Sedgwick basin (Schoewe, 1949) on a stable continental craton. The subsurface is composed of predominantly Paleozoic horizontal sedimentary layers with the oldest rocks of the Permian system (Bayne, 1960; Walters, 1961). Three strata are of interest here: (1) The Mississippian Formation, the source rock for the produced hydrocarbons and coproduced wastewater. (2) The Arbuckle Group, the deepest sedimentary layer where most of the wastewater is injected and is stratigraphically situated above the granitic basement. (3) The Precambrian basement, composed of metamorphic and igneous rocks (Merriam, 1963), where most of the induced

seismicity is located (Rubinstein et al., 2018), holds an in situ fault system, connected to the dominant geologic feature of southern Kansas, the North-East trending Nemaha Fault (Baars & Watney, 1991; McBee, 2003; Niemi et al., 2004; Steeples et al., 1979). The boundary between the Arbuckle Group and the granitic basement is between 1.7 and 2 km depth (Carr et al., 1986). In central Sumner County, several faults were observed from seismic reflection data crossing from the Arbuckle group down into the Precambrian basement (Schwab, 2016; Schwab et al., 2017), indicating the possibility of a hydraulic connection through this boundary.

Most of the seismicity in Kansas is located along the border region with Oklahoma (Rubinstein et al., 2018). Kansas had the second largest earthquake rate in the central USA after Oklahoma between 2014 and 2016. During the analyzed time period (March 2014 to December 2016), 70 high-rate wastewater injection wells were operating within the study region (Figure 1). Before 2012, the annual wastewater injection volumes were larger than 5 Mm^3 and gradually increased to reach more than 15 Mm^3 in 2014. Rubinstein et al. (2018) established several lines of evidence highlighting the link between seismicity and wastewater injection in southern Kansas. While hydraulic fracturing was also occurring in the area, no evidence of associated-induced seismicity was found (Rubinstein et al., 2018).

In this study, we employed the seismic waveform recordings and the subsequently derived seismicity catalog based on a seismic network deployed by the U.S. Geological Survey in southern Kansas, USA, starting in the year 2014 (Rubinstein et al., 2018). The seismic network was composed of 16 three-component accelerometers and 13 colocated three-component broadband seismometers operated with a sampling rate of 200 Hz. The network covered an area of 40 × 55 km in north-south and east-west directions, respectively (Figure 1). In addition, we also used stations from the Oklahoma seismic network, Central and Eastern US seismic networks and Netquakes, whenever the signal-to-noise ratio in the waveform recordings was sufficient to reliably pick the P wave first-motion polarity. Using the earthquake catalog from Rubinstein et al. (2018), we identify 5,269 earthquakes in our study area that occurred between March 2014 and December 2016 (Figure 1). Their magnitudes lie in the range $-0.3 \leq M_L \leq 5.2$. The earthquake locations were refined by the GrowClust algorithm that applied hybrid hierarchical clustering and simultaneously grouped and relocated earthquakes into several discrete clusters (Trugman & Shearer, 2017). This method is able to provide stable results for large data sets and presented here horizontal and vertical location uncertainties of 200 and 420 m under 68% confidence interval, respectively (Rubinstein et al., 2018). The magnitude of completeness M_C was 1.9 for the analyzed time period. The largest earthquakes within the studied area were the M_W 4.9 (M_L 5.2) November 12, 2014 Milan earthquake (Choy et al., 2016; Hearn et al., 2018; Joubert et al., 2020) and the M_W 4.3 October 2, 2014 Harper earthquake. The Harper earthquake occurred near the main area of wastewater disposal activities, during the period of the highest wastewater injection. In contrast, the Milan earthquake occurred at ~35 km distance from the area with the highest injection volumes, during the same time period of high fluid injection. Six additional $M_L \geq 4$ events occurred between 2014 and 2016 in the study area (see stars in Figure 1). Most of the seismicity (95% of the seismicity catalog) occurred in the shallow granitic basement between 2 and 8.5 km depth (Figure 1). Nearly, all the remaining seismicity occurred above the interpreted Arbuckle and Precambrian basement boundary suggested by Rubinstein et al. (2018) at 1.7 km depth.

The available seismicity catalog included manually picked first P wave and S wave arrival times for all signals with sufficient signal-to-noise ratio. We selected a total number of 983 seismic events with magnitudes larger than M_C in the range M_L [1.9, 5.2] and for which at least eight P wave arrival times were picked. Only events located within the footprint of seismic network were selected to secure good azimuthal coverage (Figure 1). We manually divided the 983 events into seven groups based on their epicentral distribution (Figure 2).

The signals were corrected for their instrument responses and band-pass filtered using cosine filters [0.1 1 80 100] Hz and [0.01 0.1 80 100] Hz applied to waveforms from accelerometers and broadband seismometers, respectively. We automatically determined the corresponding first-motion polarity and amplitude based on the manually picked arrival times. All waveforms were then visually reviewed to ensure the correct determination of polarities.
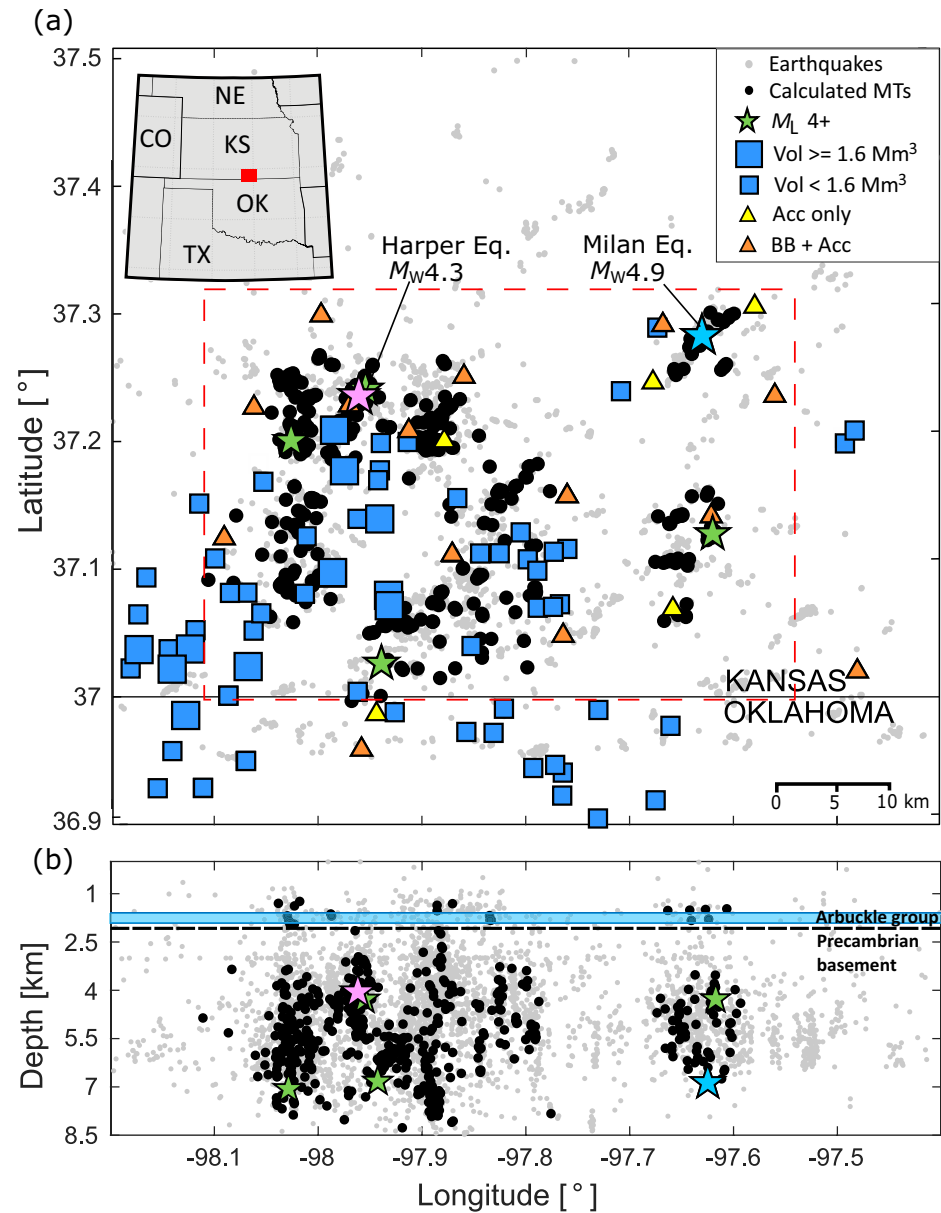
Figure 1. Locations of the 549 events (black dots) for which we calculated moment tensor solutions. Red dashed box shows study area. Gray dots represent all earthquakes from the available seismicity catalog from 2014 to 2016 with local magnitudes (M_L) in the range $-0.3 \leq M_L \leq 5.2$. Stations with accelerometers only are shown with yellow triangles, while stations with accelerometers and colocated broadband seismometers are shown with orange triangles. Note that additional seismic stations located further away from the study area were also employed but are not shown in the figure. Small and large light blue squares represent the wastewater injection wells into the Arbuckle group (Mm³ = million cubic meter) and indicate cumulative injected volume between 2014 and 2016, <1.6 Mm³ and $\geq$1.6 Mm³, respectively. $M_L \geq 4$ earthquakes are shown as stars. The blue star is the Milan earthquake, the pink star is the Harper earthquake, and the remaining stars are other $M \geq 4$ earthquakes. (a) Map view. (b) Longitude–depth profile. In (b), the dashed line represents approximate depth of the transition from Arbuckle group to the crystalline basement (Carr et al., 1986). The blue interval represents the approximate injection interval for the wastewater injection wells in the analyzed area (Rubinstein et al., 2018).
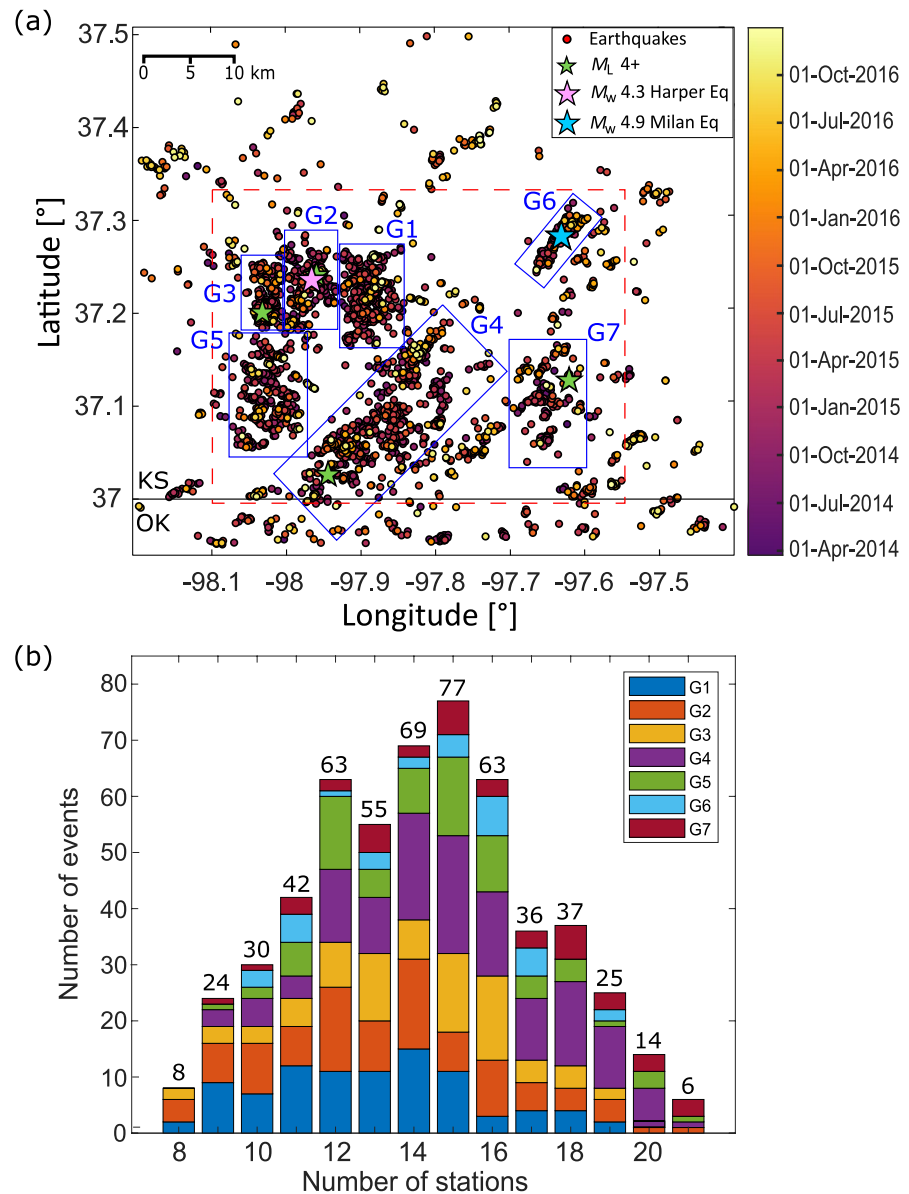
Figure 2. (a) Spatial distribution of seismicity available in the Rubinstein et al. (2018) catalog (all events) color encoded with time and locations of the seven analyzed seismicity groups (G1–G7). Red dashed box shows study area. KS, Kansas. OK, Oklahoma. (b) Histogram showing the number of stations (equal to the number of polarities and amplitudes) utilized in each event to calculate the moment tensor, and color encoded by seismicity group (G1–G7). Only the 549 events for which the moment tensors were retained are shown in the histogram.

3. Methodology

3.1. Seismic Moment Tensor Inversion

Seismic MTs are commonly used to represent the kinematic source properties of earthquakes (Frohlich, 1994; Julian et al., 1998; Vavryčuk, 2001). By inverting portions of seismograms following the onset of *P* and/or *S* wave arrivals or utilizing the first *P* wave ground displacement amplitude and the duration of the rupture process, the MT inversion illuminates the potential fault plane orientations and characterizes the partitioning of seismic deformation into pure shear (DC) and nonshear (non-DC) parts.

MTs were decomposed here into an isotropic (ISO) part and a deviatoric part. The ISO part indicates a change of volume. We further decomposed the deviatoric part of the MTs following Knopoff and Randall (1970)

dividing it into a DC part describing pure shear motion and a CLVD component. CLVD does not have a simple physical interpretation (e.g., Frohlich, 1994) but may approximately measure the nonplanarity of the activated fault plane. The full seismic MT inversion aims at resolving the following equation:

$$U = G \times M, \tag{1}$$

in which U is a vector containing the observed ground displacement amplitudes, G represents the Greens function matrix, and M is the MT with six independent components. We employed the MT inversion scheme from Kwiatek et al. (2016), which utilizes the amplitude and sign of the first-motion ground displacement P-pulse on the vertical component as a proxy to estimate the MT. We solved Equation 1 by transferring it into the optimization problem,

$$\left\| U - GM \right\|_{L1} = \min. \tag{2}$$

We used here the L1 norm, as we found it less sensitive to larger errors in the amplitude readings, providing better constrained MTs. We used the 1-D velocity model from Rubinstein et al. (2018) to estimate the takeoff angles and raypath distances at each station.

The quality of the solutions was first evaluated using the RMS error. The RMS error estimates the uncertainties of the MTs by comparing the theoretical and estimated amplitude (Stierle, Bohnhoff, et al., 2014; Stierle, Vavryčuk, et al., 2014) as follows:

$$\text{RMS} = \sqrt{\frac{\sum_{i=1}^{N}\left(U_i^{\text{obs}} - U_i^{\text{th}}\right)^2}{\sum_{i=1}^{N}\left(U_i^{\text{obs}}\right)^2}}. \tag{3}$$

After the initial inversion for the full MT as well as the DC-constrained mechanism, we retained only earthquakes for which the obtained RMS in the full inversion was ≤0.4. We manually reviewed the solutions to suppress poorly constrained mechanisms suffering from poor station coverage and/or mostly horizontal takeoff angles. This reduced the number of events to be further considered to 549.

In the next step, we applied the hybridMT technique (Kwiatek et al., 2016) separately for each of the seven manually selected seismicity groups (Figure 2). The technique takes advantage of the fact that event from the same area share similar source-station travel paths. This iterative method suppresses poorly known path/site/sensor effects, such as attenuation, near-station site effects, and improper sensor gains. Previous applications have led to improve MTs of all events within a seismicity group (Kwiatek et al., 2014; Martínez-Garzón et al., 2017). In each iteration, for each event, the observed amplitude U^{obs} was compared with the theoretical amplitude U^{th} calculated from the seismic MT solution by forming their ratio, $r = U^{\text{obs}}/U^{\text{th}}$. In the following, the ensemble of ratios from all events was used to calculate median ratio r at a given station. The observed amplitude U^{obs} was finally adjusted in the next iteration by the fraction of the observed ratio r:

$$U^{*,\text{obs}} = U^{\text{obs}} + wU^{\text{obs}}\left(r - 1\right), \tag{4}$$

where w is a weighting factor that was here set to 0.1. We used 40 iterations to refine the solutions.

We utilized the RMS (Equation 3) and the scaled maximum error of the MT components (MAXC) to evaluate the correct convergence of the MT solutions through the 40 iterations of the hybridMT inversion. The MAXC is defined as the square root of the maximum diagonal element of the MT solution covariance matrix (6×6 elements) that is normalized by the scalar seismic moment. While generally both parameters steadily decreased during the 40 iterations, some events displayed a slight increase in the RMS and MAXC errors during the last iterations. Therefore, the final solutions (both DC and full MT) for each event were selected as the solutions from the iteration with the lowest scaled MAXC.

The number of free parameters in a MT inversion varies from four for a DC-constrained MT inversion to six for a full MT inversion. As the full MT inversion has more degrees of freedom, better fit of theoretical-to-observed amplitudes can be obtained, but it does not necessarily mean that the actual solution from full MT inversion is always better. We use the Bayesian Information Criterion (BIC) (Cesca et al., 2013) to select a preferred solution (DC or full) for each earthquake:

$$BIC = k \ln(n) + n \ln(RMS/n), \tag{5}$$

in which k is the number of free MT components plus 1, n is the number of polarities employed in the inversion, and RMS is the root mean square error of the MT inversion (Kass & Raftery, 1995). For each MT, we calculated two BIC values corresponding to the DC inversion and the full MT inversion. Our preferred solution is the solution with the lowest BIC value (Supporting information Figure S1). Finally, we visually reviewed the full and DC mechanisms for each event and selected the alternative MT in some cases where the nodal planes were notably inconsistent with the polarities distribution on the focal sphere. As the P wave amplitudes are also inverted, they may dominate the inversion in some cases and result in polarity outliers. For most of these peculiar cases, full inversion was the original selected inversion and we finally selected the DC solution. Less than 10% of the final MTs were affected by this change.

Although we considered the RMS error and the takeoff angle to reject some solution previously included in the calculations and used a minimum of eight stations per event to improve the inversion quality, those parameters were not taken into account for discriminating between DC and full solutions. With respect to adding more parameters to discriminate between DC and full MTs, we tested different options, including the azimuthal gap or the number of stations. None of them resulted fully satisfactory improvements when comparing with the solutions presented by Rubinstein et al. (2018).

To evaluate whether the non-DC components of the full MTs are significant, we calculated their associated uncertainties. For each event, we generated additional 100 synthetic full MTs by randomly perturbing the input data as follows: (1) P wave amplitudes were modified up to 10%, simulating site effects or amplitude read errors (Davi et al., 2013), (2) takeoff angles were randomly perturbed up to 5°, simulating uncertainties in the velocity model up to 10%, and (3) introducing up to one incorrect polarity pick per event. For each event, we calculated the ISO% and CLVD% uncertainties as the standard deviation over the 100 synthetic MT solutions, thus representing 68% confidence interval. Considering all the MTs calculated, average uncertainties of ±13% and ±26% for the ISO% and CLVD%, respectively, were obtained under 68% confidence interval.

3.2. Stress Tensor Inversion

Utilizing the obtained MT solutions as input, we performed a stress tensor inversion to determine the local stress field orientation in the area covered by each of the seismicity groups. We also look for potential stress field variations with time and depth. To do so, we used the software package MSATSI (Martínez-Garzón et al., 2014), which estimates the stress field orientation from focal mechanisms and employs a bootstrap resampling uncertainty assessment. This package is based on the SATSI algorithm (Hardebeck & Michael, 2006), which performs a damped least squares inversion with the purpose to minimize the differences in the stress field orientations from neighboring areas. The inversion outputs are the orientation of the three principal stress axes and the relative stress magnitude R:

$$R = 1 - \frac{\sigma_2 - \sigma_3}{\sigma_1 - \sigma_3}, \tag{6}$$

in which σ_{1-3} are the magnitudes (from most to least compressive) of the three principal stress axes obtained from the deviatoric stress tensor. The relative stress magnitude R can take values between 0 and 1 and it measures whether the magnitude of the intermediate principal stress σ_2 is closer to the magnitude of the least compressive principal stress σ_3 or to the magnitude of the most compressive principal stress σ_1. The stress inversion procedure was refined to include for each of the areas an iterative stress inversion procedure following Vavryčuk (2014). In each iteration and for each focal mechanism, the fault plane better oriented for failure within the local stress field was selected for the inversion. How well oriented a fault is with respect to the local stress conditions was evaluated by means of the instability coefficient I (Lund & Slunga, 1999; Vavryčuk, 2014):

$$I = \frac{\tau - \mu(\sigma - \sigma_1)}{\tau_{opt} - \mu(\sigma_{opt} - \sigma_1)}, \tag{7}$$

Table 1
Summary of Moment Tensor Statistics Per Seismicity Group

Seismicity groups	Number of moment tensors computed	Number of events in group with $M_L \geq 1.9$	Percentage of events for which a MT was computed	Double-couple moment tensors	Full moment tensors	Full moment tensors with |ISO| < 13%	Full moment tensors with |ISO| ≥ 13%
G1	91	197	46	53 (58%)	38 (42%)	14 (15%)	24 (27%)
G2	99	199	50	46 (46%)	53 (54%)	24 (24%)	29 (30%)
G3	79	134	59	63 (80%)	16 (20%)	8 (10%)	8 (10%)
G4	135	372	36	114 (84%)	21 (16%)	7 (5%)	14 (11%)
G5	72	127	57	66 (92%)	6 (8%)	2 (3%)	4 (5%)
G6	32	78	41	17 (53%)	15 (47%)	3 (9%)	12 (38%)
G7	41	111	37	39 (95%)	2 (5%)	0 (0%)	2 (5%)
Total	549	1,218	45	398 (72%)	151 (28%)	58 (11%)	93 (17%)

Note. G1–G7 represent the seven defined seismicity groups (Figure 2). Numbers in parentheses indicate the proportion with respect to the total amount of calculated moment tensor for that group. Full moment tensors (FMTs) with \|ISO\| < 13% and FMTs \|ISO\| ≥ 13% indicate the number of FMTs with ISO% smaller and larger or equal than 13%, representing one standard deviation of the uncertainties.

where τ and σ represent the shear and normal traction vectors, respectively, μ is the friction coefficient (here set to 0.6), σ_{opt} represents the shear traction for the optimally oriented fault, and σ_1 is the magnitude of the most compressive stress axis. For details on the methodology, we refer to Vavryčuk (2014) and Martínez-Garzón, Ben-Zion, et al. (2016). A bootstrap resampling technique has been applied to characterize the 95% confidence intervals for stress-axes orientations and the relative stress magnitude (see Martínez-Garzón et al., 2014, for details).

To evaluate the evolution of the stress field orientation with depth within each seismicity group, we sorted the MTs with hypocentral depth and selected groups containing 40 events including 10 events of overlap with both neighboring groups. An equivalent procedure was applied to search for any temporal dependencies of the stress field orientation within the analyzed groups.

4. Results

4.1. Source Mechanism Analysis

A subset of 76 events from our data set was common to those calculated in Rubinstein et al. (2018). Overall, good agreement between both data sets was observed (Supporting information Text S1 and Table S1). The moment magnitudes derived from the MT inversion in this study are slightly lower but still in good agreement with those derived by Trugman et al. (2017) from spectral analysis (Supporting information Text 1 and Figure S2).

Out of the 549 manually reviewed MT solutions that we computed, based on the BIC significance test, we determined that 398 events (72% of the data set) were more appropriately represented with a DC-constrained source, while 151 events (28% of the data set) required a full MTs (Supporting information Figure S1).

We also evaluate the MTs based on whether the isotropic component was significant at a 1-standard deviation level (i.e., $\left|\text{ISO}\right| \geq 13\%$, see Section 3.1, for calculation of non-DC uncertainties). For 93 events (corresponding to 17% of the total data set), the volumetric components were found to be significant at the 68% confidence interval. Out of them, 33 events had positive ISO% representing tensile opening, and 60 events had negative ISO%, representing isotropic volume reduction. Relevant statistics for each of the seven analyzed local event groups (see Figure 2) including the number of calculated MTs, the respective proportions of DC-constrained and full MTs are provided in Table 1.

We consider 83% of the events to be consistent with DC failure because either the full MT is not significant at a 1 standard deviations confidence level or the BIC criterion indicates that the incorporation of ISO/
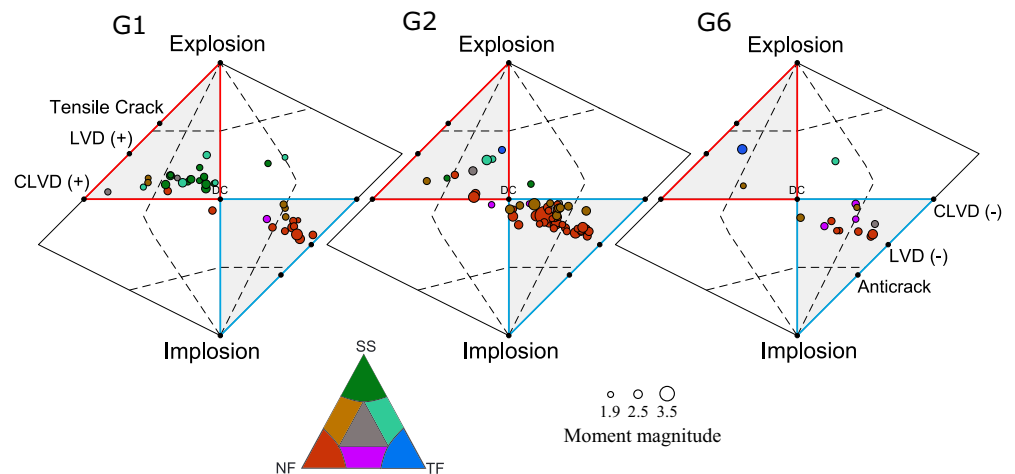
Figure 3. Source diagrams (Hudson et al., 1989) representing graphically the non-double-couple (non-DC) components of the full moment tensors from the seismicity groups G1, G2, and G6. The color indicates faulting style as determined from the ternary diagram (Frohlich, 2001). NF, normal faulting; SS, strike-slip faulting; TF, thrust faulting; CLVD, compensated linear vector dipole; LVD, linear vector dipole.

CLVD components in resolved MTs is not supported due to limited reduction of RMS errors. Among those events, considered with nonsignificant isotropic component ($|ISO| < 13\%$), only two events presented a CLVD% exceeding the average 26% and their own CLVD% uncertainty. The rest of the events presented a CLVD% smaller than the average uncertainty of 26% and for each event the CLVD% did not exceed the uncertainty of the specific event.

We were able to compute a MT for a similar proportion of the total number of earthquakes in each group (Table 1). The proportion of events with significant non-DC components shows variations from group to group. For the groups G3–G5 and G7, at least 80% of the analyzed MTs were consistent with DC sources (Table 1) and only 10% or less of the total number of MTs from each group displayed $|ISO| \geq 13\%$. The seismicity groups G2 and G6 displayed the largest proportions of events with significant non-DC components (30% and 38% respectively, see Table 1). Interestingly, these two groups contained the two largest seismic events from the catalog, the M_W 4.3 Harper and M_W 4.9 Milan earthquakes (in Figures 1 and 2). Most of the MTs from groups G2 and G6 corresponded to seismicity following the M_W 4.3 Harper and M_W 4.9 Milan earthquakes, respectively. The group G1 located directly to the east of the M_W 4.3 Harper earthquake epicenter (less than 10 km away, see e.g., Figure 2) also displayed a relatively larger proportion of non-DC components (27%, see Table 1), although slightly smaller than G2 and G6.

We visualized the non-DC included in the MTs from these three groups in diagrams following Hudson et al. (1989) (Figure 3) as well as their relation with kinematics. Normal faulting events showed predominantly negative ISO% and CLVD%, representing crack closure or compaction (Figure 3). Negative non-DC components have been observed in relation to long-term reservoir depletion from geothermal or oil production activities (e.g., Bentz et al., 2018; Dost et al., 2020; Kühn et al., 2020). In addition, a small number of strike-slip events delineating a fault structure within G1 displayed positive isotropic components signifying tensile opening (Figure 3). These events occurred during a time period of high-injection volume in G1 and could represent the opening and reactivation of a preexisting structure in the crystalline basement.

4.2. Spatial Distribution of Faulting Kinematics

We classified the 549 calculated MT solutions according to their faulting style following the color-encoding in the ternary diagram (Figure 3, after Frohlich, 2001). The ternary diagram was divided into seven regions, including normal faulting, strike-slip, reverse faulting, mixed combination from two of these faulting styles, and one oblique classification. The predominant faulting types obtained from our MT solutions were mixed normal and strike-slip, normal faulting, and strike slip, with 131, 128, and 68 mechanisms, respectively. A
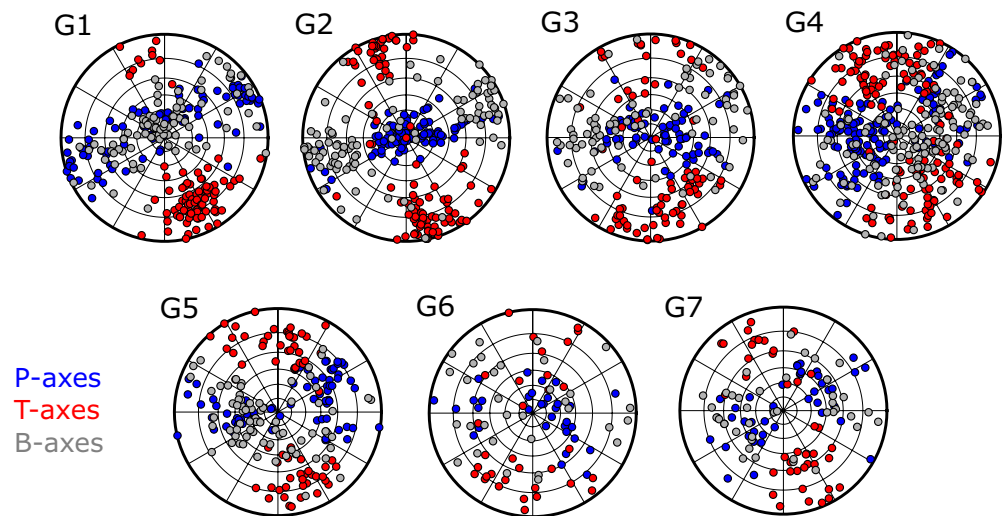
Figure 4. Lower-hemisphere stereonets displaying the direction of the compressional (P, in blue), tensional (T, in red), and null (B, in gray) axes within each of the seismicity groups.

summary of the number of events from each faulting style within each group is provided in Supporting information Table S2.

Normal faulting mechanisms were predominantly present in the northern portion of the analyzed area, including seismicity from G1 (shallower portion), G2, G3, and G6 (Figures 4 and 5 and Supporting information Table S2). This is in good agreement with diffuse fault structures with normal faulting kinematics reported in Schoenball and Ellsworth (2017) for this part of the field. Strike-slip faulting and mixed normal faulting-strike slip with (sub)horizontal P and T axes were identified mainly within G1 (deeper portion) and the southern groups G4, G5, and G7 (Figures 4 and 5 and Supporting information Table S2). The strike-slip events observed within G1 illuminated a planar structure with strike of about S80°E, which aligns well with the left-lateral nodal planes of the MTs (Figure 5c). This structure follows the well-known orientation of the nearby and northeast Humboldt fault system also striking NE-SW. However, no clear separation between the two faulting styles could consistently be identified, indicating that faults with favorable orientation to slip in normal faulting, strike-slip, or mixed faulting style might be present at local scale.

In addition, the southwestern part of the field (groups G4 and G5) displayed a larger heterogeneity in the distribution of P, T, and B axes than the other groups of seismicity and contained the largest number of mechanisms with oblique faulting kinematics (Figure 4 and Supporting information Table S2). As these two seismicity groups were closer to the area of greatest wastewater injection (Supporting information Figures S3 and S4), the larger fault mechanism heterogeneity could be linked with the stronger local stress perturbations from the wastewater injection allowing the subsequent reactivation of fault planes with a larger variety of geometries. However, no significant non-DC components were observed in this area, as one might expect from larger stress perturbations. Alternatively, the heterogeneous distribution of P, T, and B axes around G4 could simply be linked with the larger area enclosed within this group, potentially covering local stress variations.

To look for potential systematic depth changes of the predominant faulting style, we plotted all MTs with depth (Figure 6). We then formed two windows, from 2 to 5.5 km depth and from 5.5 to 8 km depth, to estimate the corresponding percentage of each faulting style with depth. Above about 5.5 km depth normal and mixed normal/strike-slip faulting accounted for 30% and 22% of the events, respectively, while pure strike-slip and mixed strike-slip/thrust faulting composed each less than 6% of the data set (Figure 6b). Below 6 km depth, an increase of strike-slip mechanisms up to 21% was observed, with the majority of the strike-slip events between 7 and 8 km depth, at the cost of decreased normal faulting kinematics (Figures 6a and 6b). Mixed normal/strike-slip and mixed strike-slip/thrust faulting slightly increased below 5.5 km depth. Below 6.5 km depth, the majority of the estimated MTs were located within the G1 area.
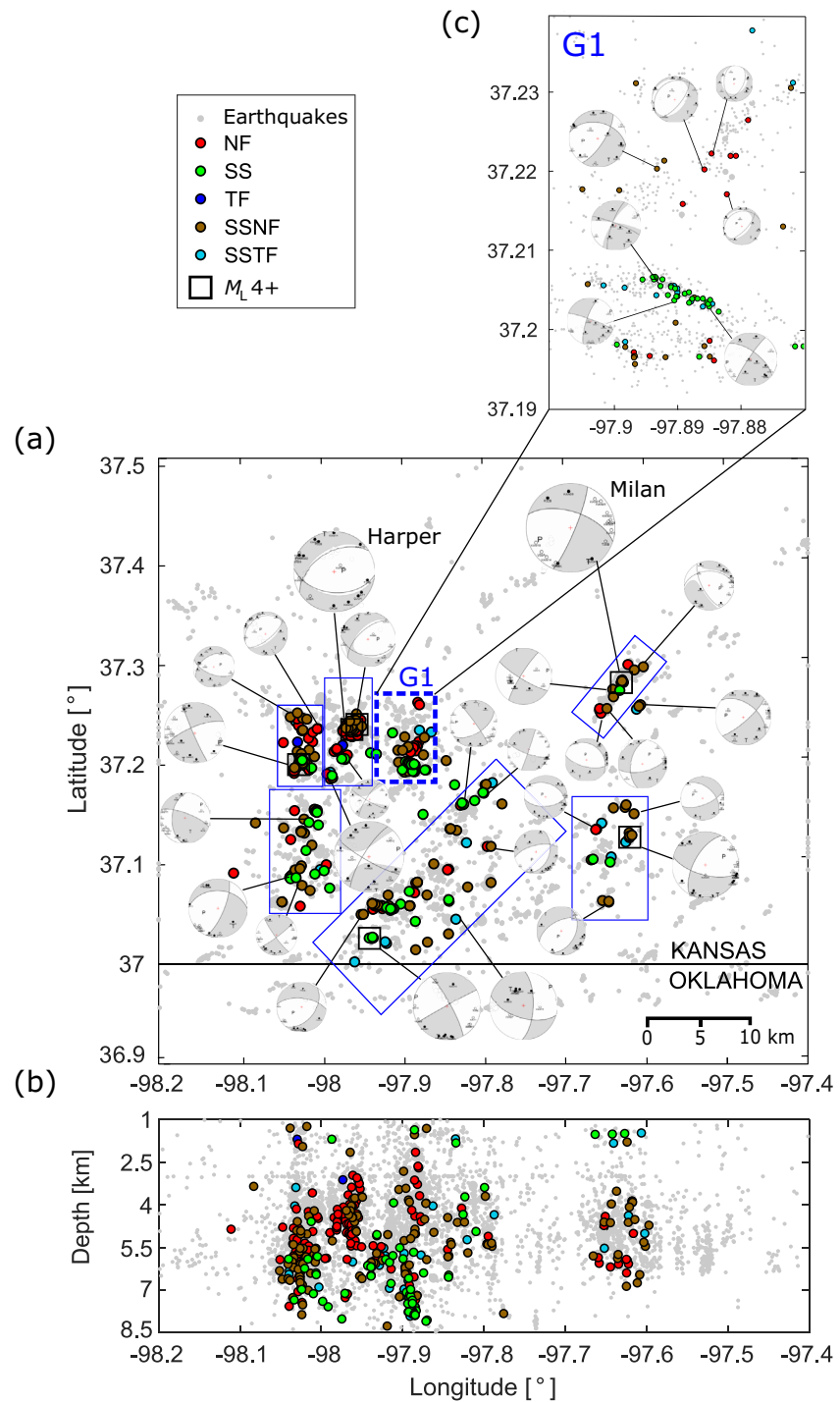
Figure 5. (a) Spatial distribution of the calculated moment tensors solutions, color encoded by their faulting style. Examples of 33 moment tensors (MTs) are shown in gray, sized with magnitude. Gray dots in the background represent all the seismicity included in the catalog. Blue rectangles indicate the seven seismicity groups (also indicated in Figure 2). (b) Same as (a) but in longitude–depth profile. (c) MT solutions from G1 highlighted a NW-SE trending fault with strike-slip faulting mechanisms and a NE-SW scattered group of normal fault(s). NF, normal faulting; SS, strike slip; TF, thrust faulting.
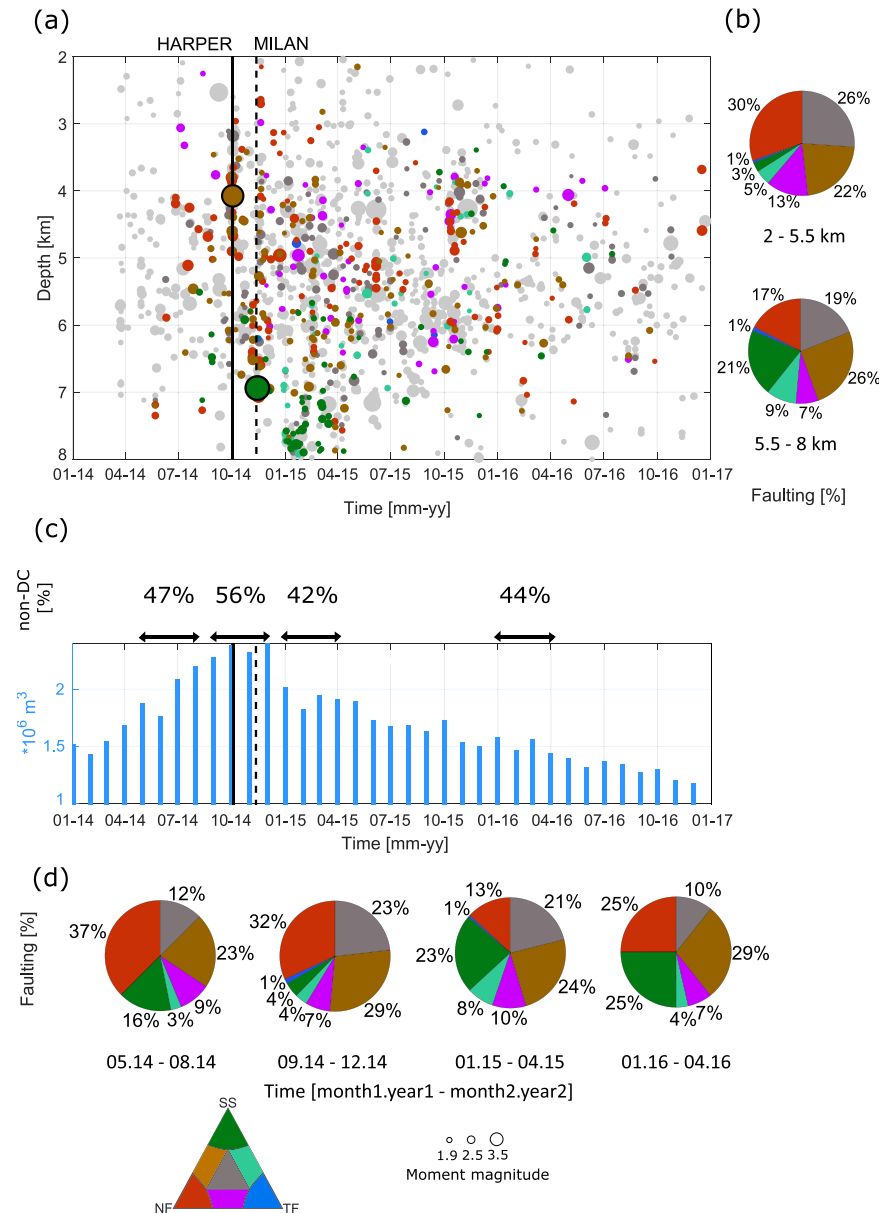
Figure 6. (a) Depth–time distribution of all the obtained moment tensor (MT) solutions. The color of the dots indicates the faulting kinematics (Frohlich, 2001) and their size is scaled with M_W. Light gray dots in the background represent all the seismicity included in the catalog. (b) Pie charts showing the proportion of faulting styles with depth for the corresponding depth range written below. Colors represent the faulting style from ternary diagram. (c) Cumulative monthly volume injected of all high-rate wastewater injection wells in the area. Magnitude of M_W 4.9 Milan and M_W 4.3 Harper earthquakes is represented in with green and brown circles, respectively. Their origin time is shown with dashed and solid vertical line. (d) Pie charts showing the proportion of faulting styles for selected time periods containing 4 months. The time frame covered in each pie chart is shown with the black horizontal arrows and their corresponding nondouble-couple (non-DC) percentages (adding both | ISO% | and | CLVD% |) in (c). Colors represent the faulting style from ternary diagram.

4.3. Temporal Evolution of Faulting Kinematics and Non-DC Components and Relation to Fluid Injection

Between the years 2014 and 2016, the total monthly injected volume through the high-rate wastewater disposal wells exceeded 1 Mm³. From July 2014 to January 2015, the injected volume reached more than 2 Mm³ per month and peaked at 2.5 Mm³ in October and December 2014 (Figure 6c). The temporal evolution of

the aggregated injection volumes through wastewater injection wells in direct vicinity or within each of the analyzed groups is correlated with the evolution of the seismicity in each of the regions (Figure 7 and Supporting information Figures S3 and S4).

Within the G1 seismicity group, spatial and temporal variations in the seismicity kinematics were observed. Normal faulting occurred throughout the entire study period mostly located between 2 and 5 km depth, while a cluster of events displaying strike-slip faulting was active between 6 and 8 km depth approximately 1 month after a peak injection in the area (Figure 7a). The strike-slip events occurred in the southern part of G1 forming an alignment approximately E-W and the normal faulting events formed a more diffuse cluster trending NW (Figure 5c). One of the nodal planes of the calculated MTs coincided well with the direction of the corresponding seismicity alignments (Figure 5c).

In October and December 2014, the M_W 4.3 Harper and M_W 4.9 Milan earthquakes occurred in G2 and G6, respectively, coinciding with the time period in which the aggregated injected volumes over the entire field were the largest (Figure 6). The Harper and Milan earthquakes also occurred during local peaks of injected volumes (Figures 7b and 7c). Within the G2 area, after the peak of injected volume in September 2014 (Figure 7b), the M_W 4.3 Harper earthquake occurred at about 4 km hypocentral depth. Eighty out of the 99 analyzed MTs from G2 corresponded to seismicity following the M_W 4.3 Harper earthquake. In the case of G6, the M_W 4.9 Milan earthquake occurred after the peak of injection in October 2014 at about 7 km hypocentral depth. Thirty out of the 32 analyzed MTs correspond to the events that occurred after the Milan earthquake. Most of the seismicity from this area displayed normal or mixed strike-slip and normal faulting and the events concentrated between 2 and 6 km depth. A downward migration of events with time was visible, highlighting the propagation of the seismicity following the M_W 4.3 Harper earthquake along the ruptured area and reflecting the migration of fluid pressure through permeable pathways in the basement (Figure 7b). Injection volumes substantially decreased after December 2014. The temporal and depth evolution of the seismicity from the other analyzed seismicity groups is provided in Supporting information Figures S3 and S4. No wastewater injection through high-rate wells was performed within the G3 and G7 groups. Within G4 and G5, largest injection volumes were also reached around October–December 2014 and substantially decreased by May–July 2015 (Supporting information Figures S3 and S4). Seismicity at the deepest portion of these groups appeared to occur after the months of maximum local injection volume (Supporting information Figures S3 and S4).

We sorted the MTs field-wide according to time, grouped them into windows of 4 months and calculated the relative contribution of each faulting style. The proportion of normal faulting events reached its maximum during the months of largest aggregated injection volume over the field (June–December 2014), composing more than 31% of the calculated MTs, while after these periods its proportion dropped to 13% in the first half of 2015 (Figures 6c and 6d). The proportion of strike-slip events varied inversely with the normal faulting events, and the strike slip reached its maximum around February 2015, during the activation of the reported deep cluster within G1 (Figure 5c). Therefore, these observations represent the activation of local portions of the field rather than a general feature field-wide.

Finally, we also calculated the proportion of non-DC components from the full MTs included in these four time intervals (Figures 6c and S6). Interestingly, the largest proportion of non-DC components (adding both | ISO% | and | CLVD% |) occurred during the period including the largest wastewater injection volumes in the region. The temporal link between the larger wastewater injection volumes and larger proportion of non-DC across the study area suggests that the stress perturbation from the fluid injection could have promoted more complex seismic ruptures resulting in larger non-DC components.

4.4. Characterization of the Local Stress Field Orientation

In the next step, we estimated the local stress field orientation within each of the analyzed seismicity groups by inverting all the obtained MT solutions from each area. The orientation of the principal stress axes and the relative stress magnitude R for each of the analyzed seismicity groups are provided in Table 2. Generally the largest and intermediate principal stresses trend ENE-WSW with distinct variations between the different groups but consistent within the error bounds. Only G2 and G4 show distinct opposite orientations of σ_1 and σ_2, representing normal stress regime and strike slip, respectively. The plunge of σ_1 and σ_2 is less
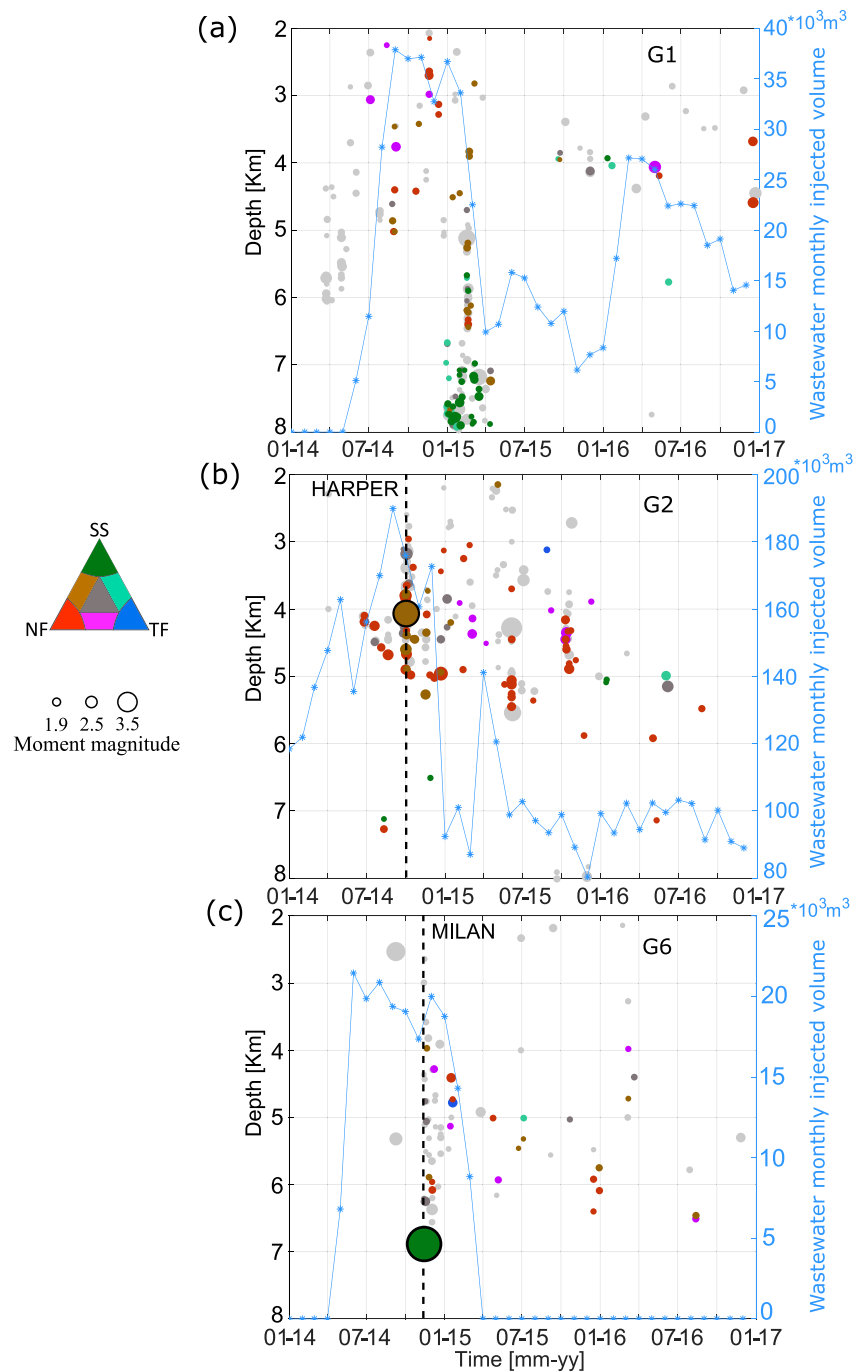
Figure 7. Depth–time distribution of moment tensors (MTs) in the seismicity groups (a) G1, (b) G2, and (c) G6. The faulting style is color encoded according to ternary diagram, and the symbol size scales with the magnitude. Blue curves represent the cumulative monthly wastewater volume injected from all injection wells located within each group. Origin time of M_W 4.3 Harper and M_W 4.9 Milan earthquakes is represented with a black vertical dashed line in (b) and (c), respectively.

Table 2
Orientation of the Local Principal Stress Axes for Each Seismicity Group

	σ_1 Trend [°]	σ_1 Plunge [°]	σ_2 Trend [°]	σ_2 Plunge [°]	σ_3 Trend [°]	σ_3 Plunge [°]	Relative stress magnitude R	Median (β) [°]	Median (I)
G1	61	13	296	69	155 [149 161]	17 [11 23]	0.12 [0 0.29]	13 [0 30]	0.96 [0.91 1]
G2	22	84	254 [248 260]	4 [−30 37]	163 [158 170]	5 [−1 45]	0.25 [0.05 0.45]	15 [0 34]	0.96 [0.86 1]
G3	59	68	265	20	172 [158 186]	9 [−2 45]	0.27 [0 0.62]	32 [0 70]	0.93 [0.84 1]
G4	249 [240 256]	35 [17 53]	72 [51 95]	55 [37 73]	340 [320 348]	2 [−42 10]	0.41 [0.18 0.62]	32 [4 60]	0.92 [0.83 1]
G5	79	36	254	54	347 [339 360]	2 [−45 11]	0.17 [0.01 0.43]	27 [8 46]	0.92 [0.83 1]
G6	88	51	280	38	185 [167 206]	6 [−13 45]	0.38 [0.04 0.77]	30 [6 54]	0.91 [0.84 0.98]
G7	251	8	35	80	160 [143 174]	6 [−11 45]	0.11 [0.01 0.58]	41 [18 64]	0.95 [0.87 1]

Note. σ_1 to σ_3 correspond to the principal stress axes characterized by their trend and plunge angles. The median (β) represents the median of the misfit angle between slip vector in each focal mechanism and the orientation of the shear traction vector. The median (I) represent the median instability parameter representing how optimally oriented a fault is with respect to the local stress field. Quantities in brackets provide with the uncertainties of each parameter under 95% confidence interval.

well determined and both confidence intervals tend to overlap in accordance with a combined normal and strike-slip (transtensional) stress field. The smallest principal stress (σ_3) is well constrained for all groups trending N-S to NNW/SSE and being subhorizontal. The recovered local stress field orientations are in good agreement with previous more general estimations of the stress field orientation in this region (e.g., Rubinstein et al., 2018; Schwab et al., 2017; Skoumal et al., 2021).

In most of the analyzed areas, the orientation of either the σ_1 or the σ_2 principal stress axis oscillated between N60°E to N89°E, except for the G6 area, where it is rotated to about S80°E (Figure 8a), therefore displaying a difference of about 25° with the other regions. The orientation of the least compressive principal stress σ_3 remains constant at S8°E–S25°E for all groups except for G6 where it is trending S5°W (Table 2).

Local variations in the stress field orientation were identified mostly for the σ_1 and σ_2 principal stress axes and the relative stress magnitude R from the different areas (Figure 8). A transtensional stress regime with $R \approx 0.15$ was observed at G1 and G5, directly to the east and south of the normal stress regime region (Figure 8) and also at G7 in the southwestern part. Finally, a strike-slip oblique stress regime was estimated for G4 approximately in the central part of the study region.

Within each group, we additionally sorted the seismicity according to depth and performed stress inversions utilizing the MTs selected by a moving depth window (see Section 3.2 for details). Most of the analyzed seismicity groups displayed a relatively constant stress field orientation with depth, except the area around G1. There, two distinct alignments of seismicity activating two different fault structures were observed (corresponding to Figure 5c), the shallower displaying mixed normal and strike-slip faulting kinematics and the deeper strike-slip faulting kinematics. Accordingly, only in G1, a change from transtensional stress regime above approximately 6 km depth to strike-slip stress regime below was observed (Figure 9a). As the majority of the MTs and strike-slip events below 6 km depth occur within G1 (see Section 4.2), this change of stress regime with depth from normal faulting to strike slip could be a local feature (see Figure 5c).

Finally, we also sorted the seismicity with time and created groups of events to invert for the stress field orientation and detect any temporal variation within the defined groups. The majority of the seismicity groups displayed a homogeneous stress field orientation with time and only G1 displayed a small change from a transtensional stress regime with $R = 0.11$ using the seismicity between July 2014 to January 2015 (coinciding with the largest injection period and the occurrence of the Harper and Milan earthquakes), to a strike-slip stress regime with $R \geq 0.17$ after that (Figures 9c and 9d). However, we note that it is not possible to recover the stress field orientation in the G2 and G6 before the Harper and Milan earthquakes, as there were not enough focal mechanisms available to perform a reliable and stable stress inversion.

One of the assumptions for a stress tensor inversion is that the stress field orientation should be homogeneous within the studied area (e.g., Gephart & Forsyth, 1984). We evaluated the difference in orientation between the stress field and the observed faults by means of the misfit angle β, measuring the angle
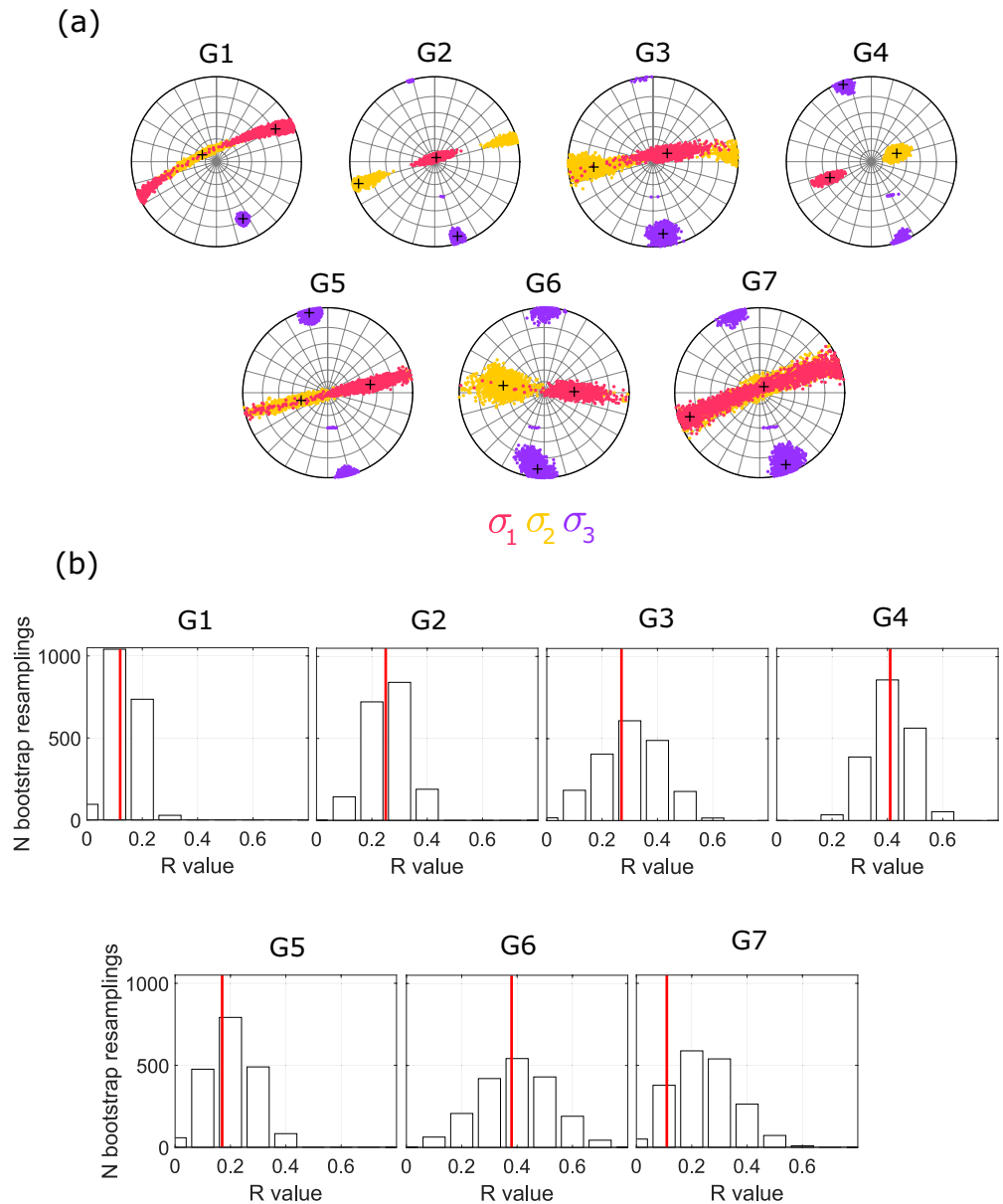
Figure 8. (a) Stereonets representing the stress field orientation for the seismicity groups G1–G7. The principal stress axes σ_1, σ_2, and σ_3 are represented in red, orange, and purple, respectively. Black crosses indicate the best solutions. Dots represent bootstrap-sampled stress-axes orientations framing the 95% confidence intervals. (b) Histograms showing the distribution of relative stress magnitudes R from the 2,000 bootstrap resampling for each seismicity group. Red line marks the R value corresponding to the best solution.

between the slip vector on each fault and the predicted shear traction vector from the stress inversion (Michael, 1991). The smallest median misfit angle β was found for G1 and G2, ($\beta \leq 15°$), indicating a relatively small fault plane variability within these areas. The largest median slip misfit β was found for G7 area ($\beta = 41$), potentially indicating larger uncertainties or larger stress heterogeneity within this area.

Although the fault parameters from the solutions from either DC or full MTs were considered, we used a stress tensor inversion method which assumes that the slip vector is projected on the fault plane (e.g., that the solution is a double couple). As we have about 17% of MTs with significant non-DC components, the results from stress inversion may suffer from it. In particular, Jia et al. (2018) have shown that neglecting the
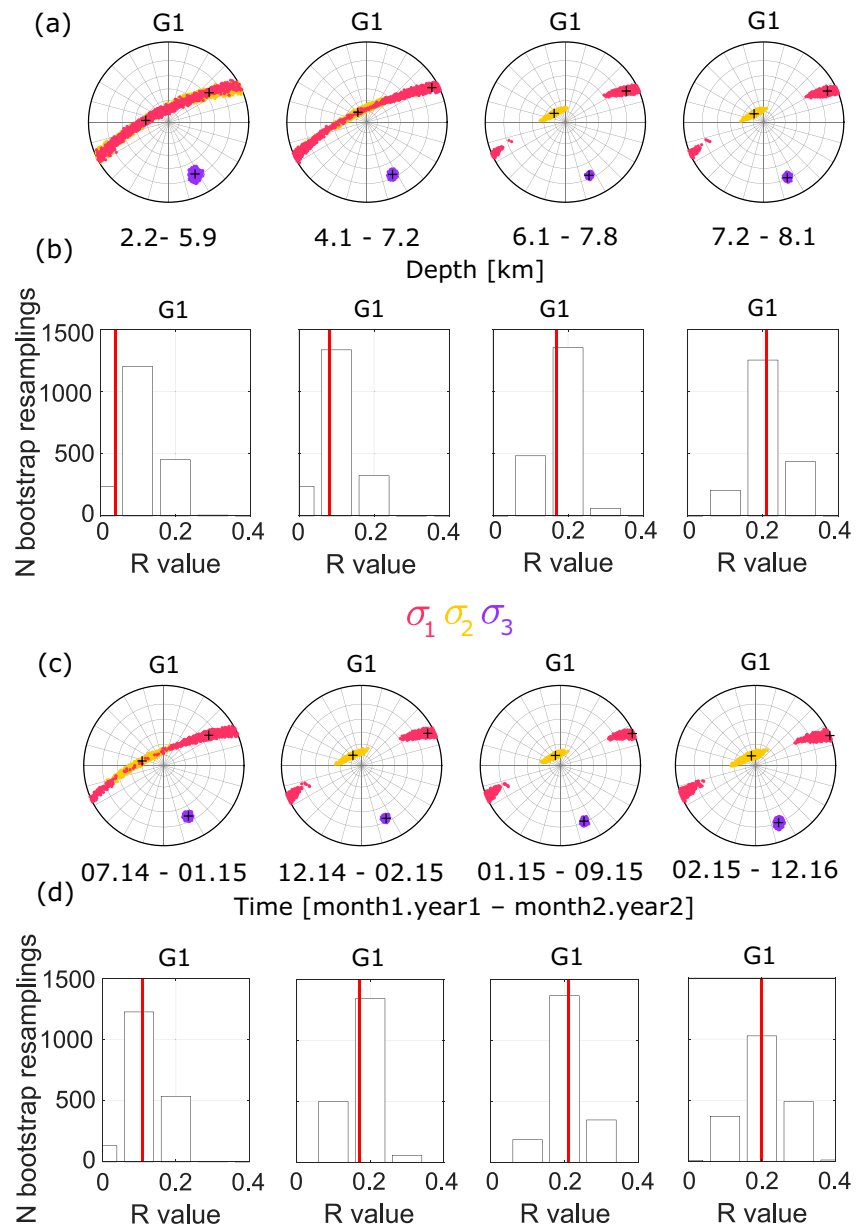
Figure 9. Evolution of the stress field orientation in the seismicity group G1 with depth (a, b) and time (c, d). (a) Stereonets representing the orientation of the three principal stress axes for selected depth intervals. The stress axes σ_1, σ_2, and σ_3 are represented in red, orange, and purple, respectively. Dots represent bootstrap-sampled stress-axes orientations framing the 95% confidence intervals. Black crosses mark the best stress orientation obtained from each of the principal stresses. (b) Histograms showing the distribution of relative stress magnitude R from bootstrap resampling. Red vertical lines indicate the best solution. (c) Same as (a) but for the time intervals. (d) Same as (b) but for the time intervals.

non-DC part of the MT increases uncertainty in the inferred principal stress axes and also leads to spurious non-Andersonian (i.e., tilted) stress axes.

4.5. Instability of the Seismically Active Faults Within Local Stress Field Orientation

The faulting kinematics of wastewater-induced seismicity in southern Kansas shows dominantly normal, strike slip, and a mix of these two (Section 4.2). In this section, we utilized the estimated instability

parameter *I* (Equation 7) determined for the preferred fault plane of each focal mechanism after the inversion (Section 3.2) to investigate how well-oriented fault planes were with respect to the local stress field orientation.

The median instability *I* values for all seven seismicity groups were larger than 0.9 (Table 2). This indicated that the majority of the retrieved fault planes along the entire analyzed area were optimally oriented for failure within their corresponding local stress conditions. Equivalent findings were observed in Oklahoma (McNamara et al., 2015; Schoenball et al., 2018; Walsh & Zoback, 2016) where small stress perturbations resulted in the reactivation of these faults (Zoback, 2007). Optimally oriented faults with respect to the local stress fields require a smaller stress change to be reactivated than faults with less favorable geometries. Therefore, this observation is in good agreement with the small proportion of non-DC components found, also indicating a small stress perturbation from the wastewater injection.

A graphical representation of the preferred nodal planes for each region within the deviatoric Mohr circle is provided in Figure 10 and Supporting information Figure S5. Within G1, the deeper earthquakes with strike-slip kinematics are better oriented to rupture under the local stress field than the shallower activated faults with normal faulting kinematics (Figure 10a).

5. Discussion

5.1. Proportion and Origin of Non-DC Components in Moment Tensors of Wastewater-Induced Seismicity

The comparison of earthquake source processes of tectonic and induced earthquakes in the US has shown a variety of results. Some studies determined that the stress drops of induced earthquakes are lower than tectonic events in the central and eastern United States (Boyd et al., 2017; Sumy et al., 2017; Trugman et al., 2017), while others have showed that tectonic and induced earthquakes have similar stress drops (Huang et al., 2017; Jeong et al., 2020; Yoshimitsu et al., 2019). MT analysis of seismicity induced by hydraulic fracturing operations revealed very small volumetric components (ISO% = 3%) (Wang et al., 2018), highlighting the similar contribution of non-DC components in tectonic and induced earthquakes. About 83% of our analyzed data set is consistent with these findings, where the source mechanisms of wastewater-induced seismic events can be well represented by a DC source mechanism and are hence comparable to those from natural earthquakes.

Still, 93 of the 549 calculated MTs had significant volumetric components $\left(\left|\text{ISO}\right| \geq 13\%\right)$. Between September 2014 and December 2014, the largest volumes of wastewater were injected into the Arbuckle, the largest proportion of earthquakes with significant non-DC components occurred as well as the two largest earthquakes (the M_W 4.3 Harper and M_W 4.9 Milan earthquakes, Figure 6) in the study period. These earthquakes occurred inside G2 and G6, which also were the groups with the largest proportion of seismicity with significant non-DC components. These two groups did not host the largest wastewater injection field-wide, although a peak in the cumulative injection volume from wells in the direct vicinity can be observed approximately around the time of the occurrence of each of these earthquakes in their corresponding area. This suggests that earthquakes with significant non-DC components tend to occur in areas or during time periods where the stress is most perturbed. To our knowledge, there is only one observation of an aftershock sequence displaying larger non-DC components (Stierle, Bohnhoff, et al., 2014). One hypothesis is that G2 and G6 could have hosted relatively lower effective stresses prior to injection so that a pore pressure change during the injection could have a relatively larger effect and also bring the optimally oriented faults to failure. However, the stress transfer from the occurrence of the larger earthquakes could have additionally perturbed locally the stress to further promote the occurrence of complex seismic ruptures.

Most of the seismicity located in the basement that appeared better characterized with full MTs displayed negative non-DC components representing compaction and/or pore collapse. The explanation of the negative volumetric components of the earthquakes is unclear. One hypothesis would be the change in mass. While there is a net mass decrease from the extraction of the oil, the size of this decrease is small because nearly all of the fluid is reinjected. Additionally, the wastewater injection takes place below the hydrocarbon production horizon, closer to the basement where the seismicity rates are the largest. Therefore, in the basement, per unit mass, the effect of wastewater injection in the Arbuckle should be larger than that of
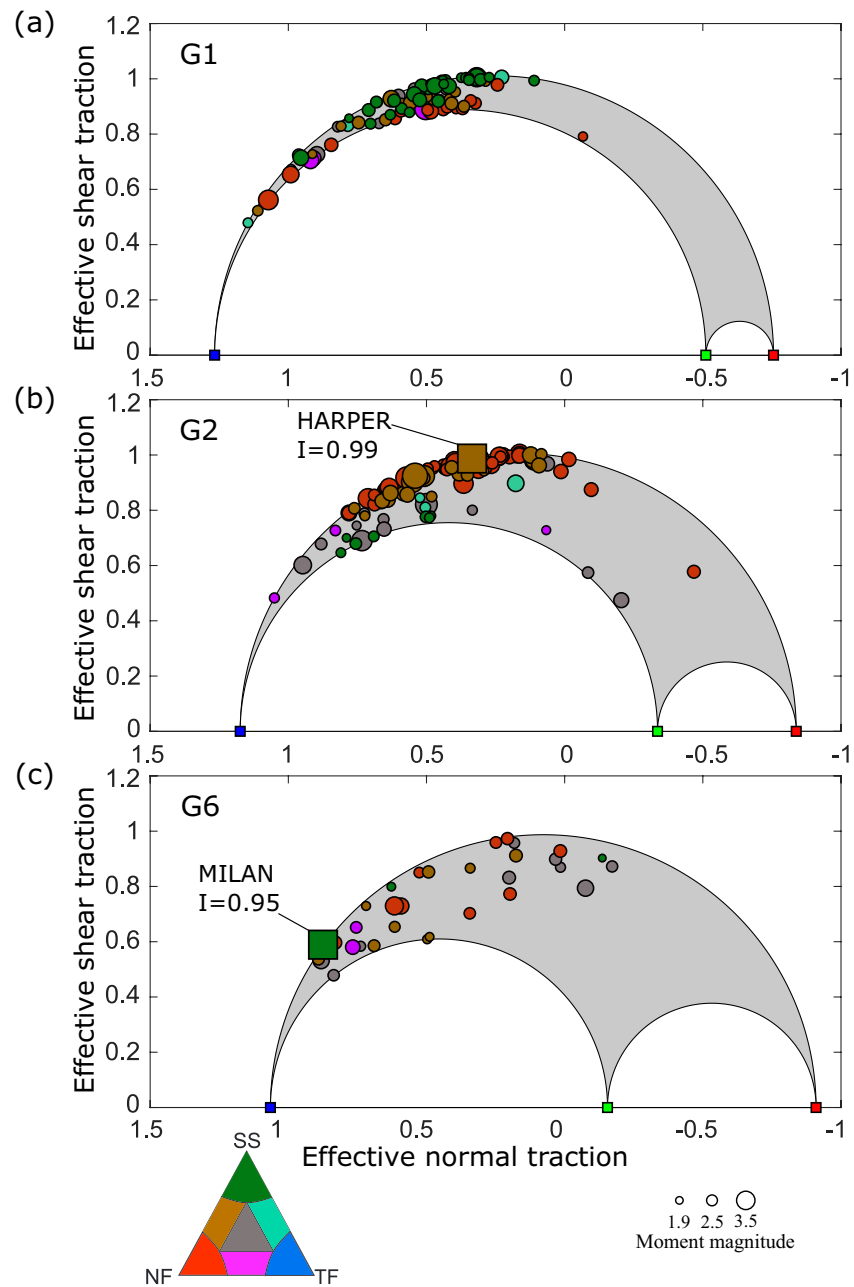
Figure 10. Mohr circles representing the effective shear and normal traction from the seismicity groups (a) G1, (b) G2, and (c) G6. The principal stress magnitudes σ_1, σ_2, and σ_3 are represented on the horizontal line as red, green, and blue squares, respectively. The circles represent the nodal planes with higher fault instability coefficient (Martínez-Garzón, Kwiatek, et al., 2016; Vavryčuk, 2014) out of the two available for each moment tensor (MT). Circles are color encoded with their faulting style according to the ternary diagram and sized with the moment magnitude. M_W 4.3 Harper and M_W 4.9 Milan earthquakes are represented as squares in (b) G2 with $I = 0.99$ and in (c) G6 with $I = 0.95$, respectively.

the extraction from the Mississippian. It is possible that despite the net mass loss, this could still result in an increase in compressive stress at depth, thus promoting compaction within the basement.

Observations of negative non-DC components in relation to reservoir depletion have been reported at the Salton Sea geothermal field, California (Bentz et al., 2018), at the Groningen oil field in the Netherlands (Dost et al., 2020; Kühn et al., 2020). Long-term depletion results in a reduction of the horizontal stresses in the reservoir and subsidence at the surface (Segall & Fitzgerald, 1998). Recently, a broad zone of

subsidence was reported to coincide with a zone of densely located injection wells in Oklahoma (Loesch & Sagan, 2018). However, more localized studies in parts of Texas and Oklahoma have shown uplift in areas of injection (Barba-Sevilla et al., 2018; Shirzaei et al., 2016; Zheng et al., 2019). In our area of interest, no study is available describing the surface displacement.

The seismicity group G1 is located directly to the East of G2 and also contained a large proportion of non-DC components (Figure 7a). Within G1, at least two local faults with different geometries and kinematics could be identified from the seismicity distribution and MTs. In the case of immature faults in a stable continental region such as those present in our study region, other additional possibilities could explain enhanced non-DC mechanisms, such as brittle damage production at the source and/or dilatant jogs created at the overlapping areas of multiple fractures (e.g., Nguyen et al., 1998; Ross et al., 2015; Zhang et al., 2016;). The positive non-DC components observed at G1 below 5.5 km depth (Figures 3a and 7a) are in agreement with this potential mechanism.

5.2. Local Stress Rotation Around the M_W 4.9 Milan Earthquake

The 2014 M_W 4.9 Milan earthquake is the largest earthquake in the study area and it ruptured far (>25 km) from the area hosting the largest wastewater injection volumes in a region where almost no seismicity was observed. Nevertheless, the earthquake occurred during a time period of high-injection volumes into local wells (Figure 7c; Choy et al., 2016).

In the G6 group including the area where the M_W 4.9 Milan earthquake occurred, we observed that the principal stress orientations are rotated clockwise of approximately 25° with respect to the neighboring regions. Skoumal et al. (2021) also examined stress in our study area based on shear wave splitting measurements and focal mechanism inversion, but any variability of the orientation of σ_{Hmax} was within the level of uncertainty (≤7°) of their measurements. The difference between our observations and those from Skoumal et al. (2021) may represent the application of different methodologies and the use of different earthquakes for focal mechanism and MT inversion. As the majority of the calculated MTs from G6 corresponded to seismicity following the M_W 4.9 Milan earthquake, the recovered stress field orientation reflects the stress field postevent. Thus, this stress field may reflect a rotation from the regional stress field due to the earthquake or it is possible that the stress field in this region was rotated with respect to the regional stress field prior to the Milan event. We find it improbable that the stress field was rotated this much across the entire G6 group because the rupture area of the Milan earthquake (approximated as a circle with radius 1.7 km by Choy et al., 2016) is significantly smaller than the size of the G6 group (~10 km in length). We find it more probable that this was a preexisting rotation of the stress field. This rotation may be the result of a weak fault within a stronger medium as has been proposed for induced earthquakes in Alberta, Canada (Igonin et al., 2021).

The fault plane instability associated with the M_W 4.9 Milan earthquake is $I = 0.95$. This instability is calculated with respect to the postevent stress field. If the pre-event stress field was notably different, this instability value may change. Assuming no large stress changes related to the M_W 4.9 earthquake, the instability value reflects the activation of a well-oriented fault, but less optimally oriented than the obtained for the M_W 4.3 Harper earthquake ($I = 0.99$). Notably, Joubert et al. (2020) argue that the Milan earthquake activated a misoriented fault within the regional stress field.

6. Summary

We calculated 549 DC and full MTs from induced seismicity associated with wastewater disposal operations in southern Kansas. We evaluated the significance of the non-DC components, and the spatiotemporal distribution of the obtained faulting kinematics, and inverted for the stress field orientation to study the activated faults and their geometries with respect to the stress field. Our main conclusions are the following:

1. Most of the events reflect pure shear (DC) faulting. Approximately 17% of the events (93 out of 549) had a significant non-DC (isotropic) component. Therefore, wastewater-induced seismicity in southern Kansas appears to have source mechanisms similar to classical crustal tectonic earthquakes to a large extent. Most of the events with significant isotropic components occurred in the areas of the M_W 4.9 Milan and

M_W 4.3 Harper earthquakes during the months of largest wastewater disposal rates, likely highlighting the areas with greater stress perturbations.

2. The predominant faulting kinematics recovered were normal faulting, strike slip, or mix of these two faulting styles. Below 6 km depth, most of the strike-slip events occur within G1 and a change from transtensional stress regime to strike-slip stress regime with depth is observed.

3. The M_W 4.9 Milan and M_W 4.3 Harper earthquakes occurred within the time period with the highest rate of active wastewater injection contained in this data set (October–December 2014). Likewise, there was an increase in the proportion of normal faulting events field-wide during the period of highest injection.

4. A transtensional stress regime is dominant with local variations toward strike-slip and normal stress regime. The orientation of the principal stress axes was relatively uniform except for the area where the M_W 4.9 Milan earthquake occurred, where the stress field appears to be rotated by about ~25°. However, it was not possible to resolve whether this rotation occurred after the earthquake, since there was very little seismicity in the area before the Milan earthquake.

5. Most of the activated fault planes presented a high instability value $I > 0.9$, indicating that they were well oriented for failure within the local stress field. The smallest median I among the analyzed groups correspond to G6, which hosted the M_W 4.9 Milan earthquake. This means that a relatively larger stress perturbation was needed in this region to bring the faults to failure.

Data Availability Statement

All waveform was accessed from the Incorporated Research Institutions for Seismology (IRIS) Data Management Center (https://iris.edu). Data from the following networks were used: GS (https://doi.org/10.7914/SN/GS), NQ (https://doi.org/10.7914/SN/NQ), N4 (https://doi.org/10.7914/SN/N4), and OK (https://doi.org/10.7914/SN/OK). Injection data can be accessed online and distributed online or in scans of paper records through the Kansas Geological Survey http://www.kgs.ku.edu/Magellan/Qualified/fluid.html (last accessed May 2020) and the Kansas Open Records Act request from the KCC (form at http://kcc.ks.gov/kora/, last accessed February 2020).

References

Atkinson, G. M., Eaton, D. W., & Igonin, N. (2020). Developments in understanding seismicity triggered by hydraulic fracturing. *Nature Reviews Earth & Environment*, *1*(5), 264–277. https://doi.org/10.1038/s43017-020-0049-7

Baars, D., & Watney, W. (1991). Paleotectonic control of reservoir facies. In *Sedimentary modeling: Computer simulations and methods for improved parameter definition. Kansas Geological Survey bulletin* (Vol. 0097-4471, pp. 253–262). Lawrence, KS: State Geological Survey of Kansas.

Barba-Sevilla, M., Baird, B. W., Liel, A. B., & Tiampo, K. F. (2018). Hazard implications of the 2016 *M*w 5.0 Cushing, OK earthquake from a joint analysis of damage and InSAR data. *Remote Sensing*, *10*(11), 1715. https://doi.org/10.3390/rs10111715

Barbour, A. J., Norbeck, J. H., & Rubinstein, J. L. (2017). The effects of varying injection rates in Osage County, Oklahoma, on the 2016 M_W 5.8 Pawnee earthquake. *Seismological Research Letters*, *88*, 1040–1053. https://doi.org/10.1785/0220170003

Bayne, C. K. (1960). Geology and ground-water resources of Harper County, Kansas. *Kansas Geological Survey Bulletin*, *143*, 183 pp.

Bentz, S., Martínez-Garzón, P., Kwiatek, G., Bohnhoff, M., & Renner, J. (2018). Sensitivity of full moment tensors to data preprocessing and inversion parameters: A case study from the Salton Sea geothermal field. *Bulletin of the Seismological Society of America*, *108*(2), 588–603. https://doi.org/10.1785/0120170203

Boyd, O. S., McNamara, D. E., Hartzell, S., & Choy, G. (2017). Influence of lithostatic stress on earthquake stress drops in North America. *Bulletin of the Seismological Society of America*, *107*(2), 856–868. https://doi.org/10.1785/0120160219

Carr, J. E., McGovern, H. E., Gogel, T., & Doveton, J. H. (1986). *Geohydrology of and potential for fluid disposal in the Arbuckle Aquifer in Kansas* (Open-File Rep. 86-491). Reston, VA: U.S. Geological Survey. https://doi.org/10.3133/ofr86491

Cesca, S., Rohr, A., & Dahm, T. (2013). Discrimination of induced seismicity by full moment tensor inversion and decomposition. *Journal of Seismology*, *17*(1), 147–163. https://doi.org/10.1007/s10950-012-9305-8

Choy, G. L., Rubinstein, J. L., Yeck, W. L., McNamara, D. E., Mueller, C. S., & Boyd, O. S. (2016). A rare moderate-sized (M_W 4.9) earthquake in Kansas: Rupture process of the Milan, Kansas, earthquake of 12 November 2014 and its relationship to fluid injection. *Seismological Research Letters*, *87*(6), 1433–1441. https://doi.org/10.1785/0220160100

Cochran, E. S., Ross, Z. E., Harrington, R. M., Dougherty, S. L., & Rubinstein, J. L. (2018). Induced earthquake families reveal distinctive evolutionary patterns near disposal wells. *Journal of Geophysical Research: Solid Earth*, *123*, 8045–8055. https://doi.org/10.1029/2018JB016270

Davi, R., Vavryčuk, V., Charalampidou, E.-M., & Kwiatek, G. (2013). Network sensor calibration for retrieving accurate moment tensors of acoustic emissions. *International Journal of Rock Mechanics and Mining Sciences*, *62*, 59–67. https://doi.org/10.1016/j.ijrmms.2013.04.004

Dost, B., van Stiphout, A., Kühn, D., Kortekaas, M., Ruigrok, E., & Heimann, S. (2020). Probabilistic moment tensor inversion for hydrocarbon-induced seismicity in the Groningen gas field, the Netherlands, part 2: Application. *Bulletin of the Seismological Society of America*, *110*(5), 2112–2123. https://doi.org/10.1785/0120200076

Ellsworth, W. L. (2013). Injection-induced earthquakes. *Science*, *341*, 142–149. https://doi.org/10.1126/science.1225942

Ellsworth, W. L., Llenos, A. L., McGarr, A. F., Michael, A. J., Rubinstein, J. L., Mueller, C. S., et al. (2015). Increasing seismicity in the U.S. midcontinent: Implications for earthquake hazard. *The Leading Edge*, *34*(6), 618–626. https://doi.org/10.1190/tle34060618.1

Frohlich, C. (1994). Earthquakes with non-double-couple mechanisms. *Science*, *264*(5160), 804–809. https://doi.org/10.1126/science.264.5160.804

Frohlich, C. (2001). Display and quantitative assessment of distributions of earthquake focal mechanisms. *Geophysical Journal International*, *144*(2), 300–308. https://doi.org/10.1046/j.1365-246x.2001.00341.x

Gephart, J. W., & Forsyth, D. W. (1984). An improved method for determining the regional stress tensor using earthquake focal mechanism data: Application to the San Fernando earthquake sequence. *Journal of Geophysical Research*, *89*(B11), 9305–9320. https://doi.org/10.1029/JB089iB11p09305

Goebel, T. H. W., Weingarten, M., Chen, X., Haffener, J., & Brodsky, E. E. (2017). The 2016 M_W5.1 Fairview, Oklahoma earthquakes: Evidence for long-range poroelastic triggering at >40 km from fluid disposal wells. *Earth and Planetary Science Letters*, *472*, 50–61. https://doi.org/10.1016/j.epsl.2017.05.011

Hardebeck, J. L., & Michael, A. J. (2006). Damped regional-scale stress inversions: Methodology and examples for southern California and the Coalinga aftershock sequence. *Journal of Geophysical Research*, *111*, B11310. https://doi.org/10.1029/2005JB004144

Hearn, E. H., Koltermann, C., & Rubinstein, J. L. (2018). Numerical models of pore pressure and stress changes along basement faults due to wastewater injection: Applications to the 2014 Milan, Kansas earthquake. *Geochemistry, Geophysics, Geosystems*, *19*, 1178–1198. https://doi.org/10.1002/2017GC007194

Huang, Y., Ellsworth, W. L., & Beroza, G. C. (2017). Stress drops of induced and tectonic earthquakes in the central United States are indistinguishable. *Science Advances*, *3*(8), e1700772. https://doi.org/10.1126/sciadv.1700772

Hudson, J. A., Pearce, R. G., & Rogers, R. M. (1989). Source type plot for inversion of the moment tensor. *Journal of Geophysical Research*, *94*(B1), 765–774. https://doi.org/10.1029/JB094iB01p00765

Igonin, N., Verdon, J. P., Kendall, J. M., & Eaton, D. W. (2021). Large-scale fracture systems are permeable pathways for fault activation during hydraulic fracturing. *Journal of Geophysical Research: Solid Earth*, *126*, e2020JB020311. https://doi.org/10.1029/2020JB020311

Jeong, S., Stump, B. W., & DeShon, H. R. (2020). Spectral characteristics of ground motion from induced earthquakes in the Fort Worth basin, Texas, using the generalized inversion technique. *Bulletin of the Seismological Society of America*, *110*(5), 2058–2076. https://doi.org/10.1785/0120200097

Jia, S. Q., Eaton, D. W., & Wong, R. C. (2018). Stress inversion of shear-tensile focal mechanisms with application to hydraulic fracture monitoring. *Geophysical Journal International*, *215*(1), 546–563. https://doi.org/10.1093/gji/ggy290

Jost, M. U., & Herrmann, R. B. (1989). A student's guide to and review of moment tensors. *Seismological Research Letters*, *60*(2), 37–57. https://doi.org/10.1785/gssrl.60.2.37

Joubert, C., Sohrabi, R., Rubinstein, J. L., Jansen, G., & Miller, S. A. (2020). Injection-induced earthquakes near Milan, Kansas, controlled by karstic networks. *Geophysical Research Letters*, *47*, E88326. https://doi.org/10.1029/2020GL088326

Julian, B. R., Miller, A. D., & Foulger, G. R. (1998). Non-double-couple earthquakes 1. Theory. *Reviews of Geophysics*, *36*(4), 525–549. https://doi.org/10.1029/98RG00716

Kass, R. E., & Raftery, A. E. (1995). Bayes factors. *Journal of the American Statistical Association*, *90*(430), 773–795. https://doi.org/10.1080/01621459.1995.10476572

Knopoff, L., & Randall, M. J. (1970). The compensated linear-vector dipole: A possible mechanism for deep earthquakes. *Journal of Geophysical Research*, *75*(26), 4957–4963. https://doi.org/10.1029/JB075i026p04957

Kühn, D., Heimann, S., Isken, M. P., Ruigrok, E., & Dost, B. (2020). Probabilistic moment tensor estimation for hydrocarbon-induced seismicity in the Groningen gas field, The Netherlands, part 1: Testing. *Bulletin of the Seismological Society of America*, *110*(5), 2095–2011. https://doi.org/10.1785/0120200099

Kwiatek, G., Charalampidou, E.-M., Dresen, G., & Stanchits, S. (2014). An improved method for seismic moment tensor inversion of acoustic emissions through assessment of sensor coupling and sensitivity to incidence angle. *International Journal of Rock Mechanics and Mining Science*, *65*, 153–161. https://doi.org/10.1016/j.ijrmms.2013.11.005

Kwiatek, G., Martínez-Garzón, P., & Bohnhoff, M. (2016). HybridMT: A MATLAB/Shell environment package for seismic moment tensor inversion and refinement. *Seismological Research Letters*, *87*, 964–976. https://doi.org/10.1785/0220150251

Kwiatek, G., Martínez-Garzón, P., Plenkers, K., Leonhardt, M., Zang, A., von Specht, S., et al. (2018). Insights into complex subdecimeter fracturing processes occurring during a water injection experiment at depth in Äspö hard rock laboratory, Sweden. *Journal of Geophysical Research: Solid Earth*, *123*, 6616–6635. https://doi.org/10.1029/2017JB014715

Loesch, E., & Sagan, V. (2018). SBAS analysis of induced ground surface deformation from wastewater injection in East Central Oklahoma, USA. *Remote Sensing*, *10*(2), 283. https://doi.org/10.3390/rs10020283

Lund, B., & Slunga, R. (1999). Stress tensor inversion using detailed microearthquake information and stability constraints: Application to Ölfus in southwest Iceland. *Journal of Geophysical Research*, *104*(B7), 14947–14964. https://doi.org/10.1029/1999JB900111

Martínez-Garzón, P., Ben-Zion, Y., Abolfathian, N., Kwiatek, G., & Bohnhoff, M. (2016). A refined methodology for stress inversions of earthquake focal mechanisms. *Journal of Geophysical Research: Solid Earth*, *121*, 8666–8687. https://doi.org/10.1002/2016JB013493

Martínez-Garzón, P., Kwiatek, G., Bohnhoff, M., & Dresen, G. (2016). Impact of fluid injection on fracture reactivation at The Geysers geothermal field. *Journal of Geophysical Research: Solid Earth*, *121*, 7432–7449. https://doi.org/10.1002/2016JB013137

Martínez-Garzón, P., Kwiatek, G., Bohnhoff, M., & Dresen, G. (2017). Volumetric components in the earthquake source related to fluid injection and stress state. *Geophysical Research Letters*, *44*, 800–809. https://doi.org/10.1002/2016GL071963

Martínez-Garzón, P., Kwiatek, G., Ickrath, M., & Bohnhoff, M. (2014). MSATSI: A MATLAB package for stress inversion combining solid classic methodology, a new simplified user-handling, and a visualization tool. *Seismological Research Letters*, *85*(4), 896–904. https://doi.org/10.1785/0220130189

McBee, W. (2003). *The Nemaha and other strike-slip faults in the midcontinent U.S.A.* Paper presented at AAPG Mid-Continent Section Meeting Proceedings, Tulsa, OK.

McKenzie, D. P. (1969). The relation between fault plane solutions for earthquakes and the directions of the principal stresses. *Bulletin of the Seismological Society of America*, *59*(2), 591–601.

McNamara, D. E., Benz, H. M., Herrmann, R. B., Bergman, E. A., Earle, P., Holland, A., et al. (2015). Earthquake hypocenters and focal mechanisms in central Oklahoma reveal a complex system of reactivated subsurface strike-slip faulting. *Geophysical Research Letters*, *42*, 2742–2749. https://doi.org/10.1002/2014GL062730

Merriam, D. F. (1963). The geologic history of Kansas. In *Kansas Geological Survey bulletin* (Vol. 162). Retrieved from http://www.kgs.ku.edu/Publications/Bulletins/162/index.html (last accessed November 2019).

Michael, A. J. (1991). Spatial variations in stress within the 1987 Whittier Narrows, California, aftershock sequence: New techniques and results. *Journal of Geophysical Research*, *96*(B4), 6303–6319. https://doi.org/10.1029/91JB00195

Moeck, I., Kwiatek, G., & Zimmermann, G. (2009). Slip tendency analysis, fault reactivation potential and induced seismicity in a deep geothermal reservoir. *Journal of Structural Geology*, *31*(10), 1174–1182. https://doi.org/10.1016/j.jsg.2009.06.012

Morris, A., Ferrill, D. A., & Henderson, D. B. (1996). Slip-tendency analysis and fault reactivation. *Geology*, *24*(3), 275–278. https://doi.org/10.1130/0091-7613(1996)024<0275:STAAFR>2.3.CO;2

Nguyen, P. T., Harris, L. B., Powell, C. M., & Cox, S. F. (1998). Fault-valve behavior in optimally oriented shear zones: An example at the Revenge gold mine, Kambalda, Western Australia. *Journal of Structural Geology*, *20*(12), 1625–1640. https://doi.org/10.1016/s0191-8141(98)00054-6

Niemi, T. M., Ferris, A. N., & Abers, G. A. (2004). Investigation of microearthquakes, macroseismic data, and liquefaction associated with the 1867 Wamego earthquake in eastern Kansas. *Bulletin of the Seismological Society of America*, *94*(6), 2317–2329. https://doi.org/10.1785/0120030101

Ross, Z. E., Ben-Zion, Y., & Zhu, L. (2015). Isotropic source terms of San Jacinto fault zone earthquakes based on waveform inversions with a generalized CAP method. *Geophysical Journal International*, *200*(2), 1269–1280. https://doi.org/10.1093/gji/ggu460

Rubinstein, J. L., Ellsworth, W. L., & Dougherty, S. L. (2018). The 2013–2016 induced earthquakes in Harper and Sumner counties, southern Kansas. *Bulletin of the Seismological Society of America*, *108*(2), 674–689. https://doi.org/10.1785/0120170209

Rubinstein, J. L., & Mahani, A. B. (2015). Myths and facts on wastewater injection, hydraulic fracturing, enhanced oil recovery, and induced seismicity. *Seismological Research Letters*, *86*(4), 1060–1067. https://doi.org/10.1785/0220150067

Schoenball, M., & Ellsworth, W. L. (2017). Waveform-relocated earthquake catalog for Oklahoma and southern Kansas illuminates the regional fault network. *Seismological Research Letters*, *88*(5), 1252–1258. https://doi.org/10.1785/0220170083

Schoenball, M., Walsh, F. R., Weingarten, M., & Ellsworth, W. L. (2018). How faults wake up: The Guthrie-Langston, Oklahoma earthquakes. *The Leading Edge*, *37*(2), 82–160. https://doi.org/10.1190/tle37020100.1

Schoewe, W. H. (1949). The geography of Kansas: Part II. Physical geography. *Transaction of the Kansas Academy of Science*, *52*(3), 261–333. https://doi.org/10.2307/3625794

Schultz, R., Skoumal, R. J., Brudzinski, M. R., Eaton, D., Baptie, B., & Ellsworth, W. (2020). Hydraulic fracturing-induced seismicity. *Reviews of Geophysics*, *58*, e2019RG000695. https://doi.org/10.1029/2019RG000695

Schwab, D. R. (2016). *Characterizing the potential for fault reactivation related to fluid injection through subsurface structural mapping and stress field analysis, Wellington Field, Sumner County, Kansas* (Master's thesis). Lawrence, KS: University of Kansas.

Schwab, D. R., Bidgoli, T. S., & Taylor, M. H. (2017). Characterizing the potential for injection-induced fault reactivation through subsurface structural mapping and stress field analysis, Wellington field, Sumner county, Kansas. *Journal of Geophysical Research: Solid Earth*, *122*, 10132–10154. https://doi.org/10.1002/2017JB014071

Segall, P., & Fitzgerald, S. D. (1998). A note on induced stress changes in hydrocarbon and geothermal reservoirs. *Tectonophysics*, *289*(1), 117–128. https://doi.org/10.1016/S0040-1951(97)00311-9

Shirzaei, M., Ellsworth, W. L., Tiampo, K. F., González, P. J., & Manga, M. (2016). Surface uplift and time-dependent seismic hazard due to fluid injection in eastern Texas. *Science*, *353*(6306), 1416–1419. https://doi.org/10.1126/science.aag0262

Skoumal, R. J., Cochran, E. S., Kroll, K. A., Rubinstein, J. L., & McPhillips, D. (2021). Characterizing stress orientations in southern Kansas. *Bulletin of the Seismological Society of America*, *111*(3). 1–10. https://doi.org/10.1785/0120200340

Steeples, D. W., DuBois, S. M., & Wilson, F. W. (1979). Seismicity, faulting, and geophysical anomalies in Nemaha County, Kansas: Relationship to regional structures. *Geology*, *7*, 134–138.

Stierle, E., Bohnhoff, M., & Vavryčuk, V. (2014). Resolution of non-double-couple components in the seismic moment tensor using regional networks—II: Application to aftershocks of the 1999 M_W7.4 Izmit earthquake. *Geophysical Journal International*, *196*(3), 1878–1888. https://doi.org/10.1093/gji/ggt503

Stierle, E., Vavryčuk, V., Šílený, J., & Bohnhoff, M. (2014). Resolution of non-double-couple components in the seismic moment tensor using regional networks—I: A synthetic case study. *Geophysical Journal International*, *196*(3), 1869–1877. https://doi.org/10.1093/gji/ggt502

Sumy, D. F., Neighbors, C. J., Cochran, E. S., & Keranen, K. M. (2017). Low stress drops observed for aftershocks of the 2011 M_w 5.7 Prague, Oklahoma, earthquake. *Journal of Geophysical Research: Solid Earth*, *122*, 3813–3834. https://doi.org/10.1002/2016JB013153

Trugman, D. T., Dougherty, S. L., Cochran, E. S., & Shearer, P. M. (2017). Source spectral properties of small to moderate earthquakes in southern Kansas. *Journal of Geophysical Research: Solid Earth*, *122*, 8021–8034. https://doi.org/10.1002/2017JB014649

Trugman, D. T., & Shearer, P. M. (2017). GrowClust: A hierarchical clustering algorithm for relative earthquake relocation, with application to the Spanish Springs and Sheldon, Nevada, earthquake sequences. *Seismological Research Letters*, *88*(2A), 379–391. https://doi.org/10.1785/0220160188

Vavryčuk, V. (2001). Inversion for parameters of tensile earthquakes. *Journal of Geophysical Research*, *106*(B8), 16339–16355. https://doi.org/10.1029/2001JB000372

Vavryčuk, V. (2011). Principal earthquakes: Theory and observations from the 2008 West Bohemia swarm. *Earth and Planetary Science Letters*, *305*(3–4), 290–296. https://doi.org/10.1016/j.epsl.2011.03.002

Vavryčuk, V. (2014). Iterative joint inversion for stress and fault orientations from focal mechanisms. *Geophysical Journal International*, *199*(1), 69–77. https://doi.org/10.1093/gji/ggu224

Walsh, F. R., & Zoback, M. D. (2015). Oklahoma's recent earthquakes and saltwater disposal. *Science Advances*, *1*(5), e1500195. https://doi.org/10.1126/sciadv.1500195

Walsh, F. R., & Zoback, M. D. (2016). Probabilistic assessment of potential fault slip related to injection-induced earthquakes: Application to north-central Oklahoma, USA. *Geology*, *44*(12), 991–994. https://doi.org/10.1130/G38275.1

Walters, K. L. (1961). *Geology and ground-water resources of Sumner County, Kansas*. In Kansas Geological Survey bulletin (Vol. 151). Retrieved from http://www.kgs.ku.edu/General/Geology/Sumner/index.html

Wang, R., Gu, Y. J., Schultz, R., & Chen, Y. (2018). Faults and non-double-couple components for induced earthquakes. *Geophysical Research Letters*, *45*, 8966–8975. https://doi.org/10.1029/2018GL079027

Weingarten, M., Ge, S., Godt, J. W., Bekins, B. A., & Rubinstein, J. L. (2015). High-rate injection is associated with the increase in U.S. mid-continent seismicity. *Science*, *348*(6241), 1336–1340. https://doi.org/10.1126/science.aab1345

Yoshimitsu, N., Ellsworth, W. L., & Beroza, G. C. (2019). Robust stress drop estimates of potentially induced earthquakes in Oklahoma: Evaluation of empirical green's function. *Journal of Geophysical Research: Solid Earth*, *124*, 5854–5866. https://doi.org/10.1029/2019JB017483

Zhang, H., Eaton, D. W., Li, G., Liu, Y., & Harrington, R. M. (2016). Discriminating induced seismicity from natural earthquakes using moment tensors and source spectra. *Journal of Geophysical Research: Solid Earth*, *121*, 972–993. https://doi.org/10.1002/2015JB012603

Zhang, H., Eaton, D. W., Rodriguez, G., & Jia, S. Q. (2019). Source-mechanism analysis and stress inversion for hydraulic-fracturing-induced event sequences near Fox Creek, Alberta. *Bulletin of the Seismological Society of America*, *109*(2), 636–651. https://doi.org/10.1785/0120180275

Zheng, W., Kim, J. W., Ali, S. T., & Lu, Z. (2019). Wastewater leakage in West Texas revealed by satellite radar imagery and numerical modeling. *Science Reports*, *9*, 14601. https://doi.org/10.1038/s41598-019-51138-4

Zoback, M. D. (2007). *Reservoir geomechanics*. Cambridge: University Press. https://doi.org/10.1017/CBO9780511586477

Reference From the Supporting Information

Kagan, Y. Y. (1991). 3-D rotation of double-couple earthquake sources. *Geophysical Journal International*, *106*(3), 709–716. https://doi.org/10.1111/j.1365-246X.1991.tb06343.x